

An alternative permeable topology design space for trailing-edge noise attenuation

Luesutthiviboon, S.; Ragni, D.; Avallone, F.; Snellen, M.

DOI

[10.1177/1475472X211003295](https://doi.org/10.1177/1475472X211003295)

Publication date

2021

Document Version

Final published version

Published in

International Journal of Aeroacoustics (online)

Citation (APA)

Luesutthiviboon, S., Ragni, D., Avallone, F., & Snellen, M. (2021). An alternative permeable topology design space for trailing-edge noise attenuation. *International Journal of Aeroacoustics (online)*, 20(3-4), 221-253. <https://doi.org/10.1177/1475472X211003295>

Important note

To cite this publication, please use the final published version (if applicable). Please check the document version above.

Copyright

Other than for strictly personal use, it is not permitted to download, forward or distribute the text or part of it, without the consent of the author(s) and/or copyright holder(s), unless the work is under an open content license such as Creative Commons.

Takedown policy

Please contact us and provide details if you believe this document breaches copyrights. We will remove access to the work immediately and investigate your claim.

An alternative permeable topology design space for trailing-edge noise attenuation

International Journal of Aeroacoustics

0(0) 1–33

© The Author(s) 2021



Article reuse guidelines:

sagepub.com/journals-permissions

DOI: 10.1177/1475472X211003295

journals.sagepub.com/home/jae

Salil Luesutthiviboon¹ , Daniele Ragni²,
Francesco Avallone² and Mirjam Snellen¹

Abstract

This study focuses upon a new permeable topology design concept as an alternative to porous metal foams, for turbulent boundary layer trailing-edge (TBL-TE) noise attenuation. The present permeable topology has unconventional characteristics with respect to the metal foams: a combination of low flow resistivity r and high form drag coefficient C . The unconventional characteristics are realized by a Kevlar-covered 3D-printed perforated structure. An experimental study featuring a NACA 0018 airfoil model with a Kevlar-covered 3D-printed TE insert at chord-based Reynolds numbers up to 4.6×10^5 is carried out. The airfoil with this TE insert gives a broadband TBL-TE noise reduction up to approximately 5 dB, compared to a solid TE. This reduction varies only slightly with airfoil loading (lower than 1 dB variation), in contrast to the porous metal foams (up to 3 dB variation). When comparing the variation of noise attenuation given by all the permeable materials considered, the variation is found to decrease with the increasing C . This is because C specifies the permeable material's ability to withstand the increasing pressure difference, which causes cross flow that might interfere with the noise attenuation mechanism. Additionally, the drag coefficients as well as the roughness noise of the airfoil equipped with the present TE insert are also significantly lower than those of the metal-foam TE, and are mostly negligible compared to the fully solid airfoil. Based on the findings, design guidelines for permeable TE are proposed: the permeable material shall have a combination of a low flow resistivity and a high form drag coefficient as well as a negligible surface roughness.

¹Section Aircraft Noise & Climate Effects (ANCE), Faculty of Aerospace Engineering, Delft University of Technology, Delft, The Netherlands

²Section Wind Energy, Faculty of Aerospace Engineering, Delft University of Technology, Delft, The Netherlands

Corresponding author:

Salil Luesutthiviboon, Section Aircraft Noise & Climate Effects (ANCE), Faculty of Aerospace Engineering, Delft University of Technology, Delft, The Netherlands.

Email: S.Luesutthiviboon@tudelft.nl

Keywords

Permeable materials, turbulent boundary layer trailing-edge (TBL-TE) noise, noise reduction, kevlar, 3D printing

Date received: 10 September 2020; accepted: 11 September 2020

Introduction

Airfoil self-noise, in the form of turbulent boundary layer trailing-edge (TBL-TE) noise,¹ is the major contributor to aerodynamic noise from wind turbines. Excessive exposure to wind turbine noise are found to cause health consequences.^{2,3} Due to this potential societal impact, in 2018, the World Health Organization has issued guidelines for wind turbine noise,⁴ recommending the day-evening-night-weighted Sound Pressure Level (SPL) to be below 45 dB. Subsequent regulations are limiting installation and operation of wind turbines close to densely populated areas.⁵ Nevertheless, wind turbine manufacturers today are capable of developing wind turbine blades with spans as large as 100 m, and with tip speeds exceeding 300 km/h.⁶ From the dimensional analysis by Curle⁷ and Ffowcs Williams and Hall,⁸ the acoustic power of the noise produced by the trailing edge of wind turbine blades scales with the fifth- to sixth-power of the relative free-stream flow speed, depending on the compactness of the airfoil with respect to the acoustic wavelengths. With wind turbines growing in size, the problem of TBL-TE noise becomes even more relevant.

Research on passive noise control strategies for TBL-TE noise has been carried out in the last decades by both industry and academic institutions.^{9–12} One of the most successful methods for attenuating the TBL-TE noise is integration of porous materials into the airfoil shape.^{13–20} In research conducted by Geyer et al.,¹⁴ it was shown that the application of porous materials over the full extent of an SD7003 airfoil could achieve up to 8 dB noise reduction for frequencies below 8 kHz when compared to the solid airfoil.

According to a recent investigation by Rubio Carpio et al.,²¹ the TBL-TE noise attenuation by such materials is obtained due to partial balancing of surface pressure fluctuations enabled by the permeability between the suction and the pressure sides. Such a mechanism was confirmed by the correlation of the near-surface velocity fluctuations between both sides across the porous metal-foam materials, measured with particle image velocimetry. This pressure-balancing mechanism weakens unsteady pressure imbalances, hence noise scattering, at the trailing edge.

Flow communication across the porous materials also causes balancing of the steady pressure difference between the suction and the pressure sides, leading to a loss of lift.²² For instance, up to 75% reduction of lift has been reported for highly permeable fully porous airfoils tested in a range of angles of attack between 12 and 24 degrees by Geyer et al.¹³ Studies from literature have, therefore, proposed to apply the permeable porous material only at the location where the TBL-TE noise is generated, i.e. as close as possible to the trailing edge. This approach gives a better compromise between the noise reduction and the preservation of the original aerodynamic performance, compared to the fully porous airfoil.^{16,19,20,23}

To date, many studies have identified links between characteristics of the porous materials to aeroacoustic characteristics of airfoils equipped with them.^{13,15,18} The permeable materials are usually characterized by their resistivity (inversely proportional to the permeability) and form drag coefficient.^{24–27} Since the form drag coefficient usually increases gradually with the increasing resistivity,^{20,28} only the latter has mostly been sufficient to be related to the aeroacoustic characteristics.^{13,15} Generally, it has been found that decreasing the resistivity, potentially by increasing the pore size of the porous materials, increases the noise attenuation. For example, an experimental investigation of Herr et al.¹⁸ featuring a DLR F16 airfoil at chord-based Reynolds numbers between 0.8×10^6 and 1.2×10^6 with a permeable TE insert made of a variety of permeable topologies, including porous aluminium and sintered fiber felt, found a clear link between the increase of the maximum TBL-TE noise attenuation (up to approximately 6 dB) and the increase of the effective pore diameter. This is because the aforementioned flow communication mechanism is better facilitated by the lower resistivity, i.e. the larger pores.²⁹ The resistivity of the porous materials could be reduced to an extent that, for some sound frequencies, the most dominant source of noise scattering no longer localizes at the airfoil trailing edge. Analysis of acoustic source maps of a partially porous NACA 0018 by Rubio Carpio et al.²¹ at a chord-based Reynolds number of 2.6×10^5 and zero-degree angle of attack revealed that when the cell diameter of the porous metal-foam TE insert increases, the apparent dominant noise source shifts more upstream of the trailing edge. The shift could be so large that, for the metal-foam inserts with the largest cell diameter investigated, the dominant noise source appears to locate at the junction between the solid and the porous extent of the airfoil.

In addition, complex dependencies of the noise attenuation with the angle of attack provided by porous airfoils have been presented by Sarradj et al.¹⁵ and Geyer et al.¹³ Generally, the ability of fully and partially porous airfoils in TBL-TE noise attenuation seems to deteriorate when the airfoil loading, i.e. angle of attack, increases.^{18,30} This deterioration appears to be more pronounced as the cell diameter of the porous topology increases.¹⁶ Aerodynamic performances also clearly depend on the resistivity of the porous material. Sarradj et al.¹⁵ showed a clear reduction of lift and an increase of drag of a fully porous SD7003 airfoil with decreasing resistivity. The latter can be attributed to the surface roughness since cellular materials (i.e. open foams, generally metallic), which often entail high surface roughness, have been used in most of the previous research works. Increasing the pore size of such materials increases the surface roughness, and hence the friction drag.¹⁸ Increasing surface roughness also introduces the so-called *roughness noise* in a range of relatively high sound frequencies.^{16,18} The frequency above which the TBL-TE noise emission of the (partially) porous airfoil exceeds that of the reference solid airfoil is generally known as the *crossover frequency*.^{16,20} For instance, Herr et al.,¹⁸ found that the crossover frequency of the TBL-TE noise emission of the partially porous DLR F16 airfoil is around 9 to 12 kHz. The crossover frequency has been found to vary inversely with the pore sizes.^{15,16,18,20}

Despite the promising noise attenuation capability of the porous materials proven by experimental results in literature, usage of such materials with large airfoils or in operating wind turbines could still be unappealing for industrial manufacturers. The permeable materials typically employed in the previous studies consist of randomized pore distribution resulting from the electrodeposition manufacturing processes.^{15,16,20} Apart from the aforementioned drag and roughness noise increase due to the rough topology, large-scale

realization, including manufacturing and maintenance, of such a complex topology could be very challenging.

More recently, simplified perforated topologies comprising of an array of straight channels linking the suction and the pressure sides of the airfoil have also been employed as another alternative to the porous (metal) foam materials.^{17,28} The investigation by Herr et al.¹⁸ discussed previously also featured a micro-perforated TE insert which could achieve a comparable noise attenuation of approximately 6 dB to more conventional porous topologies such as the porous aluminium. A similar finding has been reported by Rubio Carpio et al.²⁸ for a NACA 0018 airfoil with 3D-printed TE inserts by which, when the number of straight channels per unit area is increased in order to reach a sufficiently low level of resistivity, a comparable TBL-TE noise attenuation to that achieved by a porous metal-foam insert can be obtained. Nevertheless, care has to be taken when reducing the resistivity of such a perforated structure as tonal noise may appear. Herr et al.¹⁸ and Rubio Carpio et al.²⁸ have commonly reported tonal noise increase found in their highly permeable variants of the perforated structure. It has been hypothesized that the tonal noise is caused by vortex shedding across regions of regular perforation,^{18,31} yet this issue has not further been addressed.

The downsides of the permeable materials discussed earlier, namely the surface roughness, the applicability, and the airfoil loading dependency of the metal foams as well as the tonal noise of the perforated channels, may not be overcome by the usage of conventional homogeneous permeable materials. Previous research works have anticipated that ‘tailoring’^{18,31} the permeable material properties along the chord may mitigate issues such as the tonal noise increase. However, some issues such as the surface roughness may be mitigated only partially. As an alternative, this paper focuses on tailoring the overall permeable material property in the direction normal to the chord. An unconventional combination of the flow resistivity and form drag coefficient is proposed. The concept is realized by combining two permeable materials: a 3D-printed perforated structure covered by a Kevlar fabric. The present study focuses on the use of a highly permeable 3D-printed insert with straight channels to form a simple perforated structure. The pores directly connect regions of the suction and the pressure sides, allowing a point-to-point communication between both sides. On the other hand, a stretched Kevlar fabric, which has widely been used in aeroacoustic applications to replace hard walls of closed-section wind tunnels to allow for acoustic measurements^{32–36} due to their ability to be acoustically transparent while being aerodynamically impermeable,^{33,34} is used to cover the surface of the 3D-printed perforated structure. There are two main purposes; first, the relatively smooth texture of the Kevlar fabric is expected to mitigate the roughness noise; second, the flow-impermeable Kevlar fabric is used to cover the regular highly permeable 3D-printed pattern to prevent the tonal noise generation. Overall, this present permeable material combination is expected to provide a mixture of low resistivity (given by the highly permeable 3D-printed pattern) and high form drag coefficient (given by the Kevlar sheet). Aeroacoustic characteristics of an airfoil with Kevlar-covered 3D printed TE insert is investigated with a close comparison to two other metal-foam TE inserts of which well-established characteristics are available in literature.^{16,20,21}

This paper is structured as follows: first, the perforated 3D-printed structure with and without the Kevlar fabric is characterized for their permeability and form drag coefficients to establish a baseline trend with respect to two metal-foam materials. The airfoil model with TE inserts made of those permeable materials is tested in an open-jet anechoic wind

tunnel, subjected to a range of free-stream flow speeds and angles of attack. Quantification of the far-field noise and its variation, as well as localization of the dominant scattering noise sources, are achieved by means of microphone array beamforming. In addition, the wake survey method is employed to compare the drag coefficients of the airfoil with the different permeable TE inserts. Finally, based on the analysis of the acoustic and drag results and their links to the material properties, a general design recommendation for the permeable topology for the TBL-TE noise attenuation is given.

Materials, models, and experimental techniques

Wind-tunnel set-up and permeable TE specifications

A NACA 0018 airfoil with interchangeable permeable TE inserts was studied in the anechoic vertical wind tunnel (A-Tunnel) at Delft University of Technology (TU Delft).³⁷ The airfoil was mounted on a 400 mm × 700 mm nozzle opening via two parallel side plates. The chord c was 200 mm and the span was two times the chord. The interchangeable TE inserts made up 20% of the chord. A schematic of the set-up is shown in Figure 1.

The free-stream flow speed U_∞ in the X direction was varied between 15 and 35 m/s. The corresponding chord-based Reynolds numbers Re_c ranged from approximately 1.9×10^5 to 4.6×10^5 . For all of the flow speeds tested, the turbulence intensity was measured to be below 0.1%.^{16,37} The boundary layer was forced to turbulent by using randomly distributed 0.84 mm carborundum particles located on a 10-mm strip at $X/c = -0.8$ on both sides of the airfoil. A stethoscope was used to ensure that the boundary layer was turbulent along the entire span. Variation of the geometrical angle of attack was achieved by motor-driven

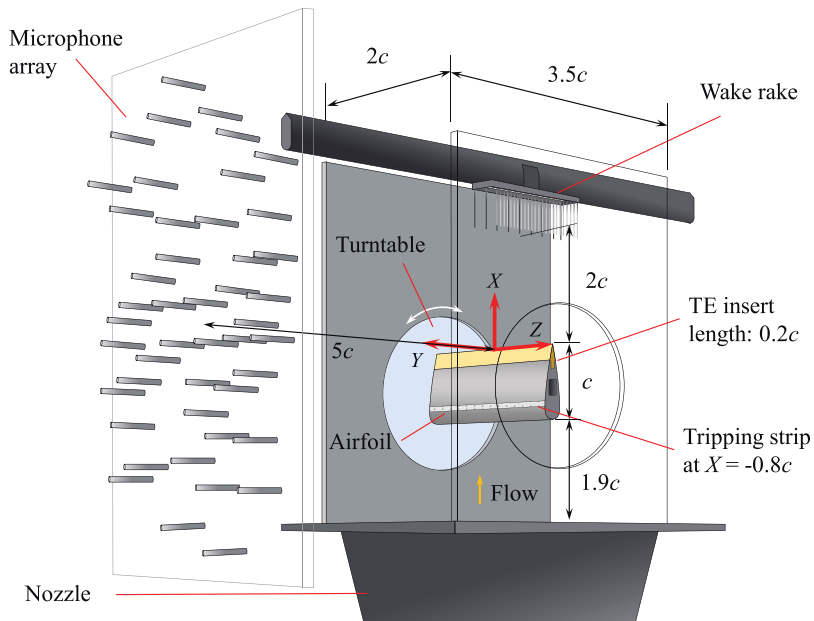


Figure 1. Schematic of the wind-tunnel test set-up, measurement devices, and coordinate system.

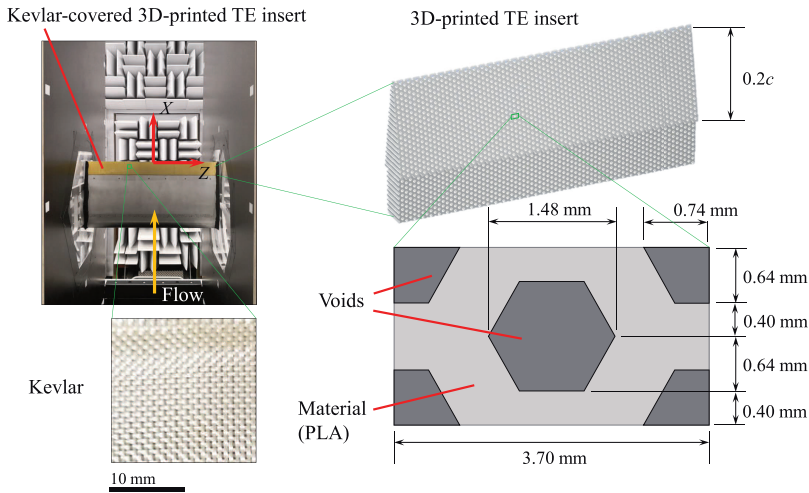


Figure 2. 3D-printed permeable TE insert covered by Kevlar installed on a NACA 0018 airfoil model with a close-up view on the Kevlar fabric, the 3D-printed TE insert, and the perforated pattern.

turntables on the side plates. The geometrical angle of attack $\alpha_{\text{geom.}}$ was varied between 0° and 24° . Data was collected most extensively at $\alpha_{\text{geom.}} = 0^\circ, 3^\circ, 6^\circ, \text{ and } 10.5^\circ$.

Figure 2 shows the 3D-printed permeable TE insert covered by the Kevlar sheet installed on the NACA 0018 airfoil model together with close-up views of the 3D-printed TE insert and the Kevlar fabric alone. The 3D-printed permeable TE insert was produced using an *Ultimaker 3* 3D printer. Polylactic Acid (PLA) was used as printing material. The honeycomb-like pattern was obtained by replicating the unit pattern shown in Figure 2. The hexagonal voids were surrounded by 0.8-mm-width 3D-printed PLA edges, forming a perforation parallel to the Y direction connecting the pressure and the suction sides of the airfoil.

The wind-tunnel tests were carried out both with and without the Kevlar sheet covering the 3D-printed TE insert. For the Kevlar-covered 3D-printed TE insert case as shown in Figure 2, the Kevlar sheet was glued to adhere on the surface of the 3D-printed permeable TE insert. The aviation-standard Kevlar 49 T 965 fabric provided by *Engineered Cramer Composites*³⁸ was used. The Kevlar foil has a weight-to-area ratio of $61 \pm 3 \text{ g/m}^2$, a density of $1.45 \pm 0.05 \text{ g/m}^3$, and a thickness of $0.12 \pm 0.02 \text{ mm}$.

Porous metal-foam TE inserts were also tested on the airfoil as baseline references. The porous metal foam made of NiCrAl was manufactured by *Alantum*, featuring dodecahedron-shaped cells. Due to the well-established characterization and experimental data in the literature, the porous metal-foam TE with a cell diameter d_c of 0.8 mm and 0.45 mm were chosen. Details on these porous metal-foam TE inserts, as well as their extensive test results can be found in previous literature.^{16,20,21}

Permeable material characterization

Characterization of the 3D-printed perforated structure with and without the Kevlar sheet was performed in order to establish a baseline trend for comparison with the

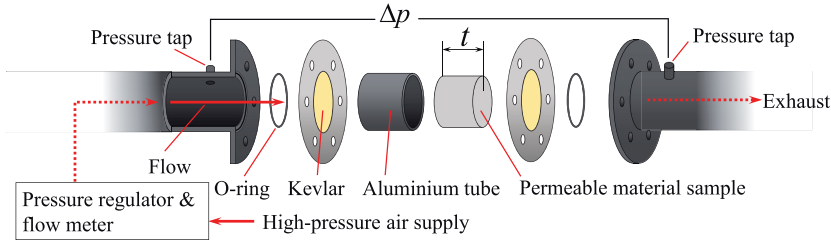


Figure 3. Exploded view of the permeability test section.

porous metal-foam materials. A cylindrical material sample made of the same material having the same perforated pattern as the TE insert was used. The diameter of the cylindrical sample was taken as 55 mm. The thickness t of the material sample was chosen to be 60 mm, according to the recommendations from previous tests.¹⁶ Characterization was done by measuring static pressure drop values across the sample. To achieve this, a high-pressure air supply of up to 10 bar was passed through an *Aventics* pressure regulator and a *TSI 4040* volumetric flow meter (range: 0 to 2.5 m/s, accuracy: 2% of reading²⁰) to reach a test section containing the material sample. An exploded view of the test section is shown in Figure 3. The 3D-printed permeable material with the pore direction aligned with the flow direction in the test section was tested with and without a stretched Kevlar sheet covering at the entrance and the exit of the permeability test section. This alignment provides a representation of the material properties across the airfoil in the direction normal to the chord, i.e. between the suction and the pressure sides.

The static pressure drop Δp across the permeability test section was measured by two pressure taps located at 50 mm up- and downstream of the section. A *Mensor 2101* differential pressure sensor (range: -1.2 to 15 kPa; accuracy: 2 Pa²⁰) was used to read the values of Δp . Fifteen different flow speed settings, controlled by the volumetric flow meter, in terms of the *Darcy velocities* v_d (defined as $v_d = Q/A$, where Q is the volumetric flow rate and A is the cross-sectional area) from 0 to 1.2 m/s were used to obtain the corresponding values of Δp .

The characteristics of the material are coefficients of the so-called *Forchheimer equation*²⁵ or the *Hazen-Dupuit-Darcy equation*²⁷ which is a quadratic equation describing Δp as a function of v_d as

$$\frac{\Delta p}{t} = \frac{\mu}{K} v_d + \rho C v_d^2 = r v_d + \rho C v_d^2 \quad (1)$$

where μ is the dynamic viscosity of the fluid, K is the *permeability*, ρ is the density of the fluid, C is the *form drag coefficient*, and r is the *flow resistivity*. These properties have widely been used in previous studies^{13,14,21,31} for permeable material characterization. Extensive explanation of equation (1) can further be found in literature.^{24–26,39}

Microphone array for acoustic measurement

Acoustic signals were recorded using an array of 64 *GRAS 40PH* microphones (frequency response ± 1 dB; frequency range: 10 Hz to 20 kHz; maximum output: 135 dB ref. 2×10^{-5}

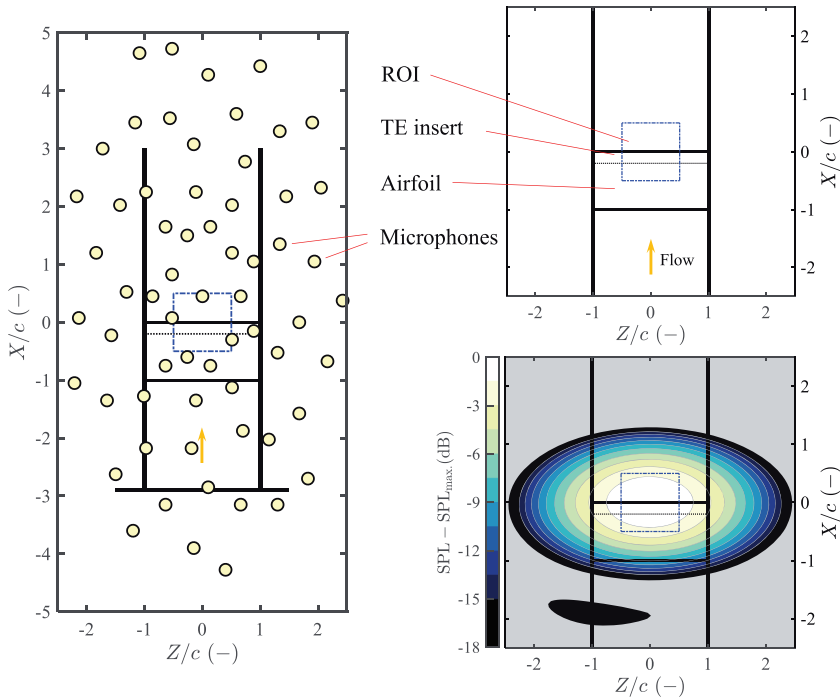


Figure 4. Schematic of the microphone array and the ROI locations relative to the NACA 0018 airfoil model. The source map shows a point spread function at 1 kHz of a point source placed at the origin.

Pa^{20}) arranged in an optimized multi-arm spiral configuration,^{40,41} see Figure 4 (left). The array plane was placed parallel to the X - Z plane shown in Figure 1. The coordinate of the central microphone was $(X, Y, Z) = (0.45c, 5c, 0)$. The sampling time per case was 20 seconds with a sampling frequency of 51.2 kHz. The Cross-Spectral Matrix (CSM) of the signal was obtained by averaging the CSMs constructed from snapshots of the time-domain signal, weighted by the Hanning weighing function. Each snapshot contained 5120 samples, yielding the final frequency resolution of 10 Hz. The $5c \times 5c$ scan plane was defined with a step of 10 mm between adjacent scan grid points, centering at the origin of the coordinate system shown in Figure 1.

The Rayleigh resolution limit⁴² regulates the minimum distance where two sound sources can still be discerned. For the present set-up, the Rayleigh resolution limit for the intended 1/3-octave band frequency range for beamforming is expected to range from $0.44c$ to $1.75c$ in the streamwise (X) direction.

Conventional Frequency-Domain Beamforming (CFDBF)⁴³ was first applied to reveal the acoustic source map. Then, in order to accurately extract only the TBL-TE noise from the source map, the source power integration (SPI) method⁴⁴⁻⁴⁶ was employed where the Region of Integration (ROI) was defined as shown in Figure 4. The ROI covers only half of the span in order to avoid the possible corner sources.^{44,46} In addition, the SPLs below -6 dB relative to the maximum SPL in the CFDBF source map at each frequency were rejected from the integration to avoid inclusion of side lobes. Having obtained the source power, the SPLs were calculated using the reference distance of 1 m, meaning that the presented SPLs

are as observed at $Y = 1$ m. A source map of a simulated point source emitting white noise placed at $(X, Y, Z) = (0, 0, 0)$ in a 1/3-octave frequency band centered at 1 kHz is also depicted in Figure 4. For this simulated point source, it can be seen that the main lobe of the point spread function is axis-symmetric with respect to the X and Z axes. In addition, the maximum sidelobe, locating far from the integration region, has the relative SPL, compared to the main lobe, lower than -15 dB which is much lower than the integration bound used in the SPI beamforming.

Drag coefficient measurements

A wake survey was performed using a traversing wake rake to measure momentum deficits and thus extract the profile drag coefficients c_D of the NACA 0018 airfoil model with different TE inserts.^{47,48} The wake rake consisted of 50 and 12 total and static pressure probes, respectively. The total pressure probes spanned a distance of $1.1c$. The probe spacing varied from 3 to 12 mm (smaller spacing in the middle). The static pressure probes were uniformly distributed with a spacing of 12 mm. Pressure data was acquired by *HoneyWell TruStability* differential pressure transducers (accuracy: 3 Pa, sampling frequency: 2 kHz). The wake rake was positioned at $X = 2c$ and traversed between $Z = -0.15c$ and $Z = 0.35c$. The center of the wake rake was adjusted according to the geometrical angle of attack such that it was aligned with the trailing edge and the momentum-deficit region in the wake was well contained within the wake rake span. The expression used to determine c_D based on the wake profile is given in equation (4).

Effective angle of attack determination

Since the tests were conducted in an open-jet wind tunnel, the effective angle of attack α_{eff} may substantially deviate from the geometrical of attack α_{geom} .⁴⁹ This section discusses the method used to determine the relationship between α_{eff} and α_{geom} for this particular set-up.

It is assumed that the relationship between α_{eff} and α_{geom} is given by

$$\alpha_{\text{eff}} \approx k_B(\alpha_{\text{geom}} + \epsilon) \quad (2)$$

where $0 < k_B < 1$ is a correction factor, an analytical expression of which is given by Brooks et al.,⁴⁹ and ϵ is an angle offset.

Static surface pressure distribution data, collected by 30 pressure taps having a diameter of 0.4 mm distributed on the airfoil surface, was used to determine α_{eff} . The pressure taps cover $-0.99 \leq X/c \leq -0.34$ on both sides of the airfoil and were connected to the same pressure scanner system as the wake rake described in the previous section. The pressure distributions at $\alpha_{\text{geom}} \leq 10.5^\circ$, and $Re_c = 4.0 \times 10^5$ and 4.6×10^5 were compared to the predicted pressure distributions from XFOIL.⁵⁰ A direct search for k_B and ϵ was used, the Sum of Squared Error (SSE) between the actual pressure distribution and that of XFOIL was collected for each combination of k_B and ϵ . Only a portion of pressure distribution upstream of the tripping strip was considered in the SSE minimization.

A contour map illustrating the SSEs for different combinations of k_B and ϵ is given on the left plot of Figure 5. The lowest SSE was obtained at $k_B = 0.67$ and $\epsilon = 0.23^\circ$. It is also

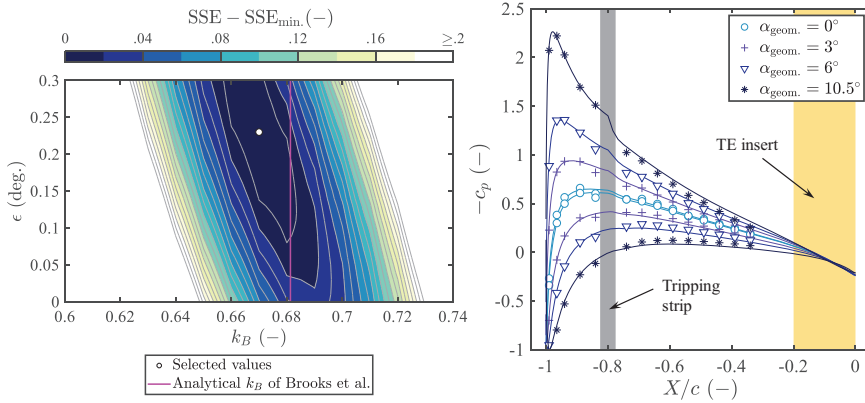


Figure 5. Left: contour plot visualizing the SSEs between the measured pressure distribution and the pressure distribution resolved by XFOIL for different combinations of k_B and ϵ . Right: pressure distribution on the NACA 0018 airfoil at $Re_c = 4.6 \times 10^5$ compared to the predictions from XFOIL after the determined values of k_B and ϵ have been applied.

found that the obtained value of k_B is very close to the analytical value ($k_B = 0.68$) for this particular setup using the formulation of Brooks et al..⁴⁹

On the right plot in Figure 5, the pressure distributions at four different $\alpha_{geom.}$ are shown and compared with the pressure distribution predicted by XFOIL (with the previously determined values of k_B and ϵ applied) in solid lines. The data was obtained when the solid TE insert is installed on the airfoil and $Re_c = 4.0 \times 10^5$. A good agreement is obtained, especially within the region between the leading edge and the tripping strip.

For the remainder of this paper, data from the four $\alpha_{geom.}$ presented in Figure 5 will mainly be discussed. For simplicity, data will be presented in terms of $\alpha_{geom.}$.

Results and discussion

Permeable material characteristics

A plot showing the measured static pressure drop Δp across the 3D-printed perforated Polylactic Acid (PLA) material sample having the thickness $t = 60$ mm with and without the Kevlar sheet for 15 different Darcy velocities v_d is shown in Figure 6 (left). The curves obtained by fitting the measured data to equation (1) to determine the air flow resistivity r , the permeability K , and the form drag coefficient C , are also given in solid and dashed lines. The resulting r , K , and C are given in Table 1. The parameters obtained from metal-foam samples with the same thickness t from the previous studies are also provided for comparison.

For the perforated 3D-printed PLA sample without the Kevlar sheet, a relatively low static pressure drop is observed, resulting in the lowest r . This is mainly due to the alignment of the straight pores with the flow direction in the permeability test section which facilitates the air flow. On the other hand, the 3D-printed perforated material sample with the Kevlar sheet shows an increase of the static pressure drop as well as a higher sensitivity of the static pressure drop with the increasing v_d . This results in an increase of r and a drastic increase of

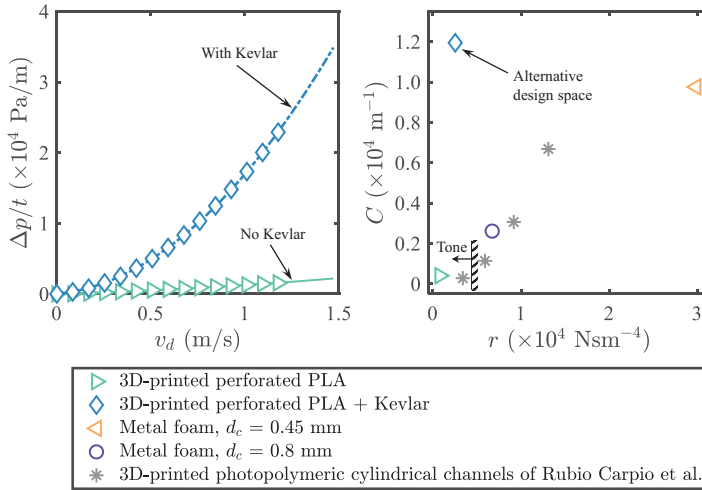


Figure 6. Left: measured static pressure drop Δp across the 3D-printed perforated PLA samples having the thickness $t = 60$ mm with and without the Kevlar sheet for 15 different Darcy velocities v_d , including the curve-fitting of equation (1) to the measured data. Right: measured r versus C for the permeable material samples tested and those from permeable materials in literature.

Table I. Measured properties of the permeable material samples and metal-foam materials.

Material sample	r (Nsm ⁻⁴)	K ($\times 10^{-10}$ m ²)	C (m ⁻¹)
3D-printed perforated PLA	787	233	404
3D-printed perforated PLA + Kevlar	2,537	72	11,945
Metal-foam, $d_c = 0.45$ mm ^{20,21}	29,850	6	9,758
Metal-foam, $d_c = 0.8$ mm ^{20,21}	6,728	27	2,613

the form drag coefficient C , the coefficient of v_d^2 in equation (1), which dictates the dependence of the static pressure drop on v_d .

A scatter plot visualizing the measured r and C of the permeable material samples tested and those from the metal-foam samples is given in Figure 6 (right). Apart from the present (Kevlar-covered) 3D-printed perforated material and metal-foam samples, the values of r and C of multiple 3D-printed photopolymeric cylindrical channel samples used in the work of Rubio Carpio et al.^{28,31} are also shown. It is important to note that, for these particular cases, the material sample thickness t is 10 mm instead of 60 mm. Nevertheless, the values of r and C , if the thickness t would be 60 mm, are not likely to differ drastically from the values shown since t is already much larger than the pore sizes and cell diameters.¹⁶ Thus, the relative trends are still worth being compared to the present materials. The readers are referred to the original publication^{28,31} for detailed specifications of these particular material samples. For the 3D-printed perforated material without the Kevlar sheet as well as the metal-foam materials, the increase of C seems to correlate with the increase of r in a similar fashion. The increase of C with respect to r for the 3D-printed photopolymeric material having cylindrical channels also appears to follow the aforementioned trend in a slightly less

gradual manner. Distinctively, the 3D-printed perforated material with the Kevlar sheet is far different from this trend; for a relatively low value of r , the value of C is around the same order of the metal foam sample with $d_c = 0.45$ mm, which has the highest r . This means that the application of the Kevlar sheet on a highly permeable 3D-printed perforated topology creates a rather unconventional combination of r and C .

The present topology of the 3D-printed perforated material sample with and without the Kevlar sheet give lower values of r than the lowest value of r found in the collection of 3D-printed photopolymeric materials. In the literature,²⁸ tonal noise increase by the airfoil equipped with the 3D-printed TE insert with the lowest r has been reported, suggesting that there exists a threshold of r below which the tonal noise would occur. The location of this threshold lies somewhere between the case with the lowest r and the case next to it, where the tonal noise was no longer found. An approximated location of this threshold is also illustrated in Figure 6 (right). Thus, in the present investigation, one could certainly expect the airfoil equipped with the 3D-printed perforated trailing-edge insert without the Kevlar sheet to also produce the tonal noise. However, for the 3D-printed perforated insert with the Kevlar sheet, despite also having a lower value of r than the identified threshold, production of the tonal noise is less certain. This is because the high value of C which does not follow the aforementioned general trend may play a role. Noise emission characteristics of the airfoil equipped with these materials as permeable trailing-edge inserts are investigated in the coming sections.

Narrow-band noise spectra

The measured narrow-band SPL spectra (frequency resolution of 10 Hz) at $Re_c = 2.6 \times 10^5$ and 4.6×10^5 , both at $\alpha_{\text{geom.}} = 0^\circ$ and 10.5° , of the airfoil with the solid TE, the 3D-printed perforated TE inserts with and without the Kevlar sheet, as well as the metal-foam TE inserts are shown in Figure 7. An alternative frequency axis is also given in terms of the non-dimensional Strouhal number based on the displacement thickness at the trailing edge on the suction side of the solid NACA 0018 airfoil $St_{\delta_s^*|_{\text{TE,ref.}}}$, where $\delta_s^*|_{\text{TE,ref.}}$ represents the displacement thickness of the boundary layer at the trailing edge (TE) on the suction side of the solid (reference) NACA 0018 airfoil, calculated by XFOIL,⁵⁰ i.e. $St_{\delta_s^*|_{\text{TE,ref.}}} = (f\delta_s^*|_{\text{TE,ref.}})/U_\infty$. Calculation with XFOIL was done by setting a forced transition at the same chordwise location $X/c = -0.8$ as on the actual airfoil on both the suction and the pressure sides. In previous studies, frequency scaling with $\delta_s^*|_{\text{TE,ref.}}$ has been found to provide a good collapse of the spectra,¹ and a good agreement between $\delta_s^*|_{\text{TE,ref.}}$ calculated from XFOIL and the actual value has been demonstrated.^{10,20,51} In addition, for each Re_c , a spectrum of the measured empty test section noise, i.e. without the airfoil, obtained by the identical beamforming methodology is also shown.

Comparing the spectra with the measured noise from the empty test section, a signal to noise ratio between 5 and 15 dB is obtained up to $f \approx 3$ kHz. Above this frequency, the signal to noise ratio is lower. Therefore, it is motivated to exclude the portion of the spectra above 3 kHz in further analysis of this paper.

For the metal-foam TEs, up to 10 dB broadband attenuation at low frequencies as well as a broadband noise increase at high frequencies are observed. The magnitudes of noise attenuation and noise increase follow the dimension of the cell diameter d_c . As explained in previous studies, increasing d_c reduces the flow resistivity r (see the previous section)

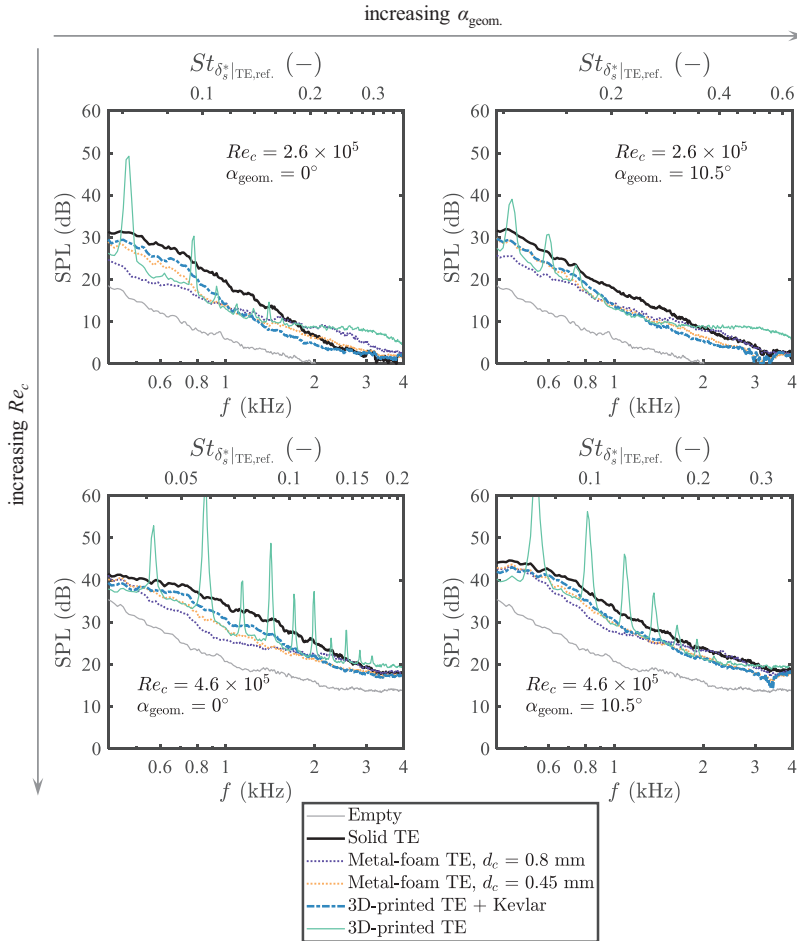


Figure 7. Narrow-band SPL spectra of the NACA 0018 airfoil with various permeable TE inserts at different given combinations of chord-based Reynolds numbers and geometrical angles of attack, compared to the reference solid TE insert and empty test section background noise.

which in turns increases noise attenuation.^{18,29} However, increasing d_c also increases surface roughness which results in the increasing roughness noise at high frequencies.^{13,15,18,21}

For the 3D-printed perforated TE insert without the Kevlar sheet, despite having a broadband noise attenuation compared to the solid counterpart, a series of strong tonal peaks are observed as anticipated. In addition, noise increase due to roughness at high frequencies can also be seen. The magnitude of the roughness noise is higher than that given by the metal-foam TE with the largest d_c , thus implying the 3D-printed permeable TE has a higher equivalent roughness than that of the metal foam. This is reasonable since the hexagonal 3D-printed pore has a larger diameter than the largest d_c of 0.8 mm of the metal foam. Additionally, the pores extend to the opposite side of the airfoil, creating a much larger effective depth than the pore cells in the metal foams.

When the Kevlar sheet is applied on the 3D-printed perforated insert, the tonal peaks as well as the roughness noise are mitigated. A broadband noise reduction of approximately 5 dB with respect to the solid TE is observed. The spectra of the Kevlar-covered 3D-printed perforated TE insert case seem to be comparable to those of the metal-foam TE insert with $d_c = 0.45$ mm; the Kevlar-covered 3D-printed perforated TE insert gives approximately 2 dB less noise attenuation at low frequencies and 2 dB more roughness noise attenuation at high frequencies. Noticeably, despite having much lower flow resistivity r than the metal-foam material with $d_c = 0.45$ mm, the Kevlar-covered 3D-printed TE does not give additional noise attenuation compared to this metal foam case. This suggests that the ranking according to r may not be a good indicator of the ranking of noise attenuation when permeable materials with different topologies are considered altogether.²⁸ In the upcoming sections, dependency of noise attenuation magnitude on different material characteristics is further discussed to identify a better indicator for noise attenuation based on the permeable material characteristics.

Interestingly, although the value of r for the Kevlar-covered 3D-printed permeable material is lower than the threshold below which the tonal noise is expected, the material has a high value of C , and, evidently, this characteristic helps to mitigate the tonal noise. Therefore, with a slight modification, it is possible to still maintain a low value of r while preventing the tonal noise. One possible way is by increasing the form drag coefficient C across the permeable topology, e.g. by applying the Kevlar sheet on the surface.

To further address the tonal noise, the spectra from the 3D-printed perforated TE without the Kevlar sheet are exclusively examined. The highly permeable 3D-printed perforated pattern may cause a sudden streamwise impedance jump, creating effectively a blunt trailing edge¹ at the junction between the solid and the permeable part of the airfoil at $X/c = -0.2$. This could promote tonal noise resulting from vortex shedding.^{18,31} Figure 8 shows exclusively the measured spectra of the 3D-printed perforated TE insert case, from which the

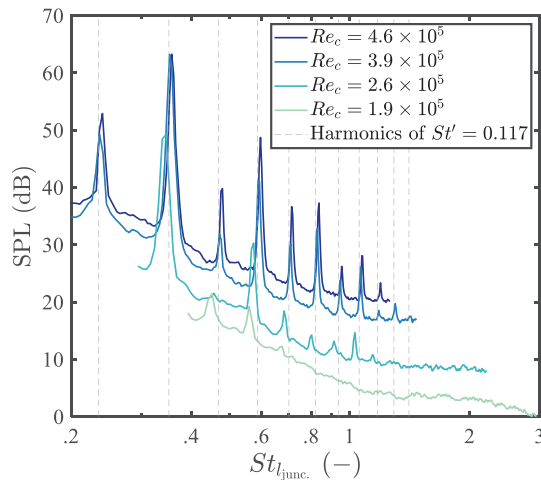


Figure 8. Narrow-band SPL spectra of the NACA 0018 airfoil with the 3D-printed perforated TE insert at different chord-based Reynolds numbers and zero-degree geometrical angle of attack presented in terms of the Strouhal number based on the thickness of the airfoil at $X/c = -0.2$, together with vertical lines marking harmonics of the fundamental Strouhal number.

tonal noise is produced, for all the Re_c considered at $\alpha_{\text{geom.}} = 0^\circ$. The frequencies are non-dimensionalized to Strouhal numbers based on the thickness of the airfoil at the junction $St_{l_{\text{junc.}}} = fl_{\text{junc.}}/U_\infty$, where $l_{\text{junc.}} = 16\text{ mm}$ is the thickness of the airfoil at $X/c = -0.2$. Noticeably, the tonal peaks from all the Re_c collapse. The fundamental Strouhal number $St' \approx 0.117$ has been found by linear regression analysis³¹ of the tonal peaks ($R^2 = 0.9975$). This value is in line with the peak Strouhal number between 0.11 and 0.17 anticipated by Brooks et al.¹ for the blunt trailing edge noise. The harmonics of St' are marked by the vertical lines which show good alignments with the tonal peaks. The presence of the vortex shedding is confirmed by the wake survey to be presented in Figure 18. However, due to the presence of the tonal noise, the 3D-printed perforated TE insert case without the Kevlar is excluded in the upcoming noise analysis in 1/3-octave bands.

Broadband noise attenuation and variability with angle of attack

To further highlight the broadband attenuation of TBL-TE noise, Figure 9 shows the values of $\Delta\text{SPL}_{1/3}$ which are the difference between the 1/3-octave SPL of each case and the 1/3-octave SPL of the solid TE (reference) case, i.e. $\Delta\text{SPL}_{1/3} = \text{SPL}_{1/3} - \text{SPL}_{1/3,\text{ref.}}$. Thus the positive and negative values of $\Delta\text{SPL}_{1/3}$ represent noise increase and noise attenuation, respectively. The values of $\Delta\text{SPL}_{1/3}$ are shown for $Re_c = 2.6 \times 10^5$ and 4.6×10^5 , at $\alpha_{\text{geom.}} = 0^\circ$ and 10.5° . An alternative non-dimensional frequency axis in terms of $St_{\delta_s^*|_{\text{TE.ref.}}}^*$ is also given in the same manner as in Figure 7.

For $\alpha_{\text{geom.}} = 0^\circ$, the noise attenuation trend follows what has been discussed in Figure 7. Maximum noise reduction of approximately 9 dB at $St_{\delta_s^*|_{\text{TE.ref.}}}^* \approx 0.06$ and 6 dB at $St_{\delta_s^*|_{\text{TE.ref.}}}^* \approx 0.1$ are found for the metal-foam TE insert cases with $d_c = 0.8$ and 0.45 mm, respectively. Observably, the higher the noise attenuation, the more variation of $\Delta\text{SPL}_{1/3}$ with the frequency, and the lower the frequency (i.e. Strouhal number) where the maximum noise attenuation occurs. For the Kevlar-covered 3D-printed TE insert, the maximum noise reduction of 3-5 dB is seen at a slightly higher $St_{\delta_s^*|_{\text{TE.ref.}}}^* \approx 0.12$. Among the permeable TE inserts considered, the Kevlar-covered 3D-printed TE insert appears to give the lowest roughness noise increase at high frequencies.

When $\alpha_{\text{geom.}}$ increases to 10.5° , the magnitudes of the maximum noise attenuation given by the metal-foam TE insert in the frequency range considered reduce by approximately 4 dB and 2 dB, for $d_c = 0.8$ mm and 0.45 mm, respectively, meaning that at when the angle of attack increases, the metal foams become relatively less effective in noise attenuation. In other words, there is a *variability* of noise attenuation by the metal-foam TE insert with the increasing angle of attack, and the variability is larger when d_c is larger. This observation is in line with a previous study.¹⁶ Interestingly, the Kevlar-covered 3D-printed TE exhibits around 1 dB variability, i.e. less than that of the metal foams.

To address the noise attenuation variability, let ΔOSPL denote the difference between the Overall Sound Pressure Level (OSPL) of a considered case and the reference solid TE case, i.e. $\Delta\text{OSPL} = \text{OSPL} - \text{OSPL}_{\text{ref.}}$, the variability of ΔOSPL with the angle of attack is taken as the relative value between ΔOSPL at a particular geometrical of attack $\alpha_{\text{geom.}}$ and that at the lowest geometrical angle of attack $\alpha_{\text{geom.,min.}}$. For convenience, a parameter $V_{\Delta\text{OSPL}}^{\alpha_{\text{geom.}}}$ is used to denote this variability, where

$$V_{\Delta\text{OSPL}}^{\alpha_{\text{geom.}}} = \Delta\text{OSPL} - \Delta\text{OSPL}_{\alpha_{\text{geom.,min.}}} \quad (3)$$

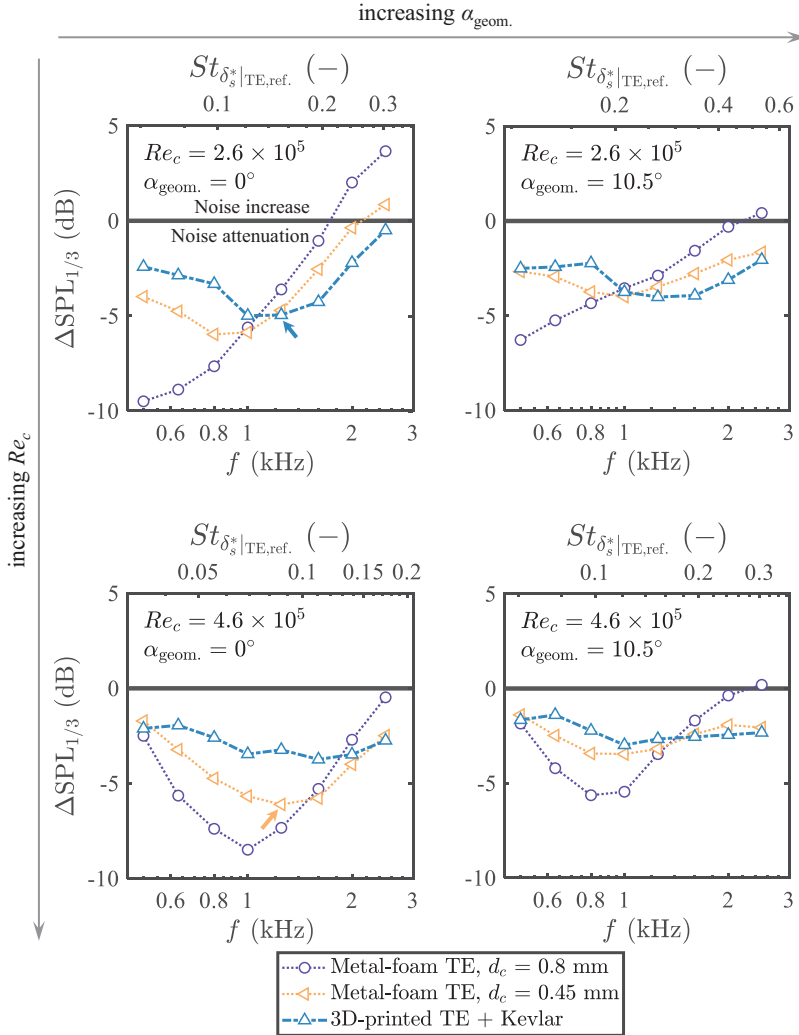


Figure 9. 1/3-octave band SPL spectra of various permeable TE inserts at different combinations of chord-based Reynolds numbers and geometrical angles of attack relative to those of the reference solid TE case ($\Delta SPL_{1/3} = SPL_{1/3} - SPL_{1/3,ref.}$).

Thus, by definition, a positive value of $V_{\Delta OSPL}^{z_{geom.}}$ represents a less effective noise attenuation capability than at $\alpha_{geom.,min.}$. As an attempt to exclude the contribution of the roughness noise increase, summation of $\Delta SPL_{1/3}$ to obtain the OSPL is done only when $\Delta SPL_{1/3} < 0$, i.e. at the sound frequencies where noise attenuation is achieved.

Examination of $V_{\Delta OSPL}^{z_{geom.}}$ of the permeable TE inserts is given in Figure 10 between $Re_c = 2.6 \times 10^5$ and 4.6×10^5 . The trend confirms the noise attenuation variability up to 3 dB for the metal-foam TE insert cases for the range of $\alpha_{geom.}$ considered. The variability is larger for a larger d_c . The minimum noise reduction variability (lower than 1 dB) is found for the Kevlar-covered 3D-printed TE. Noticeably, the magnitude of $V_{\Delta OSPL}^{z_{geom.}}$ seems to vary

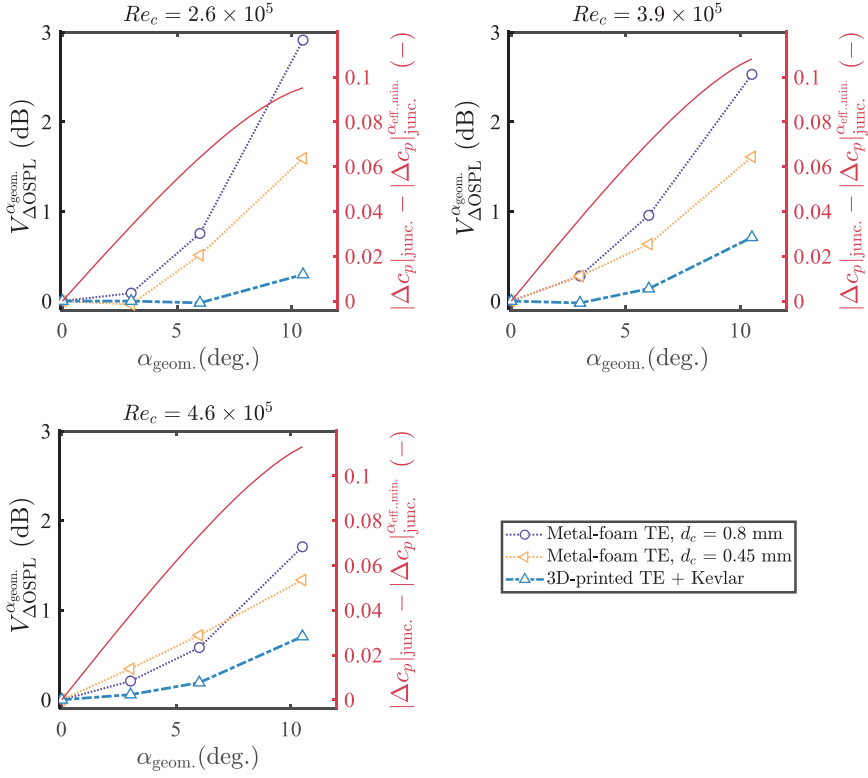


Figure 10. Noise reduction variability with respect to the angle of attack of various permeable TE inserts at different chord-based Reynolds numbers relative to the noise reduction at zero-degree geometrical angle of attack.

inversely with the form drag coefficient C of the permeable material used, i.e. the higher C , the lower $V_{\Delta\text{OSPL}}^{\alpha_{\text{geom.}}}$. This is likely because when $\alpha_{\text{geom.}}$ increases, a stronger pressure gradient between the suction and the pressure sides is present. To illustrate this, the curves showing the pressure gradient between the suction and the pressure sides of the airfoil at the junction between the solid and the permeable extent $|\Delta c_p|_{\text{junc.}}$, where ‘junc.’ denotes the chordwise location of this junction ($X/c = -0.2$), calculated from XFOIL⁵⁰ are also given Figure 10. These results are associated to the right vertical axes. The increase of the pressure gradient may induce cross flow through the permeable material. This cross flow is likely to reduce the effectiveness of the pressure balancing mechanism²¹ which contributes to the noise attenuation. Therefore, since the value of C indicates the ability of the material to withstand the cross flow resulting from the pressure gradient,²⁶ the noise attenuation capability provided by a permeable material with a larger C will have a lower tendency to become less effective when the angle of attack, i.e. the pressure gradient, increases.

Similarly, an increase of $|\Delta c_p|_{\text{junc.}}$ can also be seen as the chord-based Reynolds number Re_c increases as visualized in Figure 11, where the noise attenuation variability with Re_c , $V_{\Delta\text{OSPL}}^{Re_c}$, is examined. The definition of $V_{\Delta\text{OSPL}}^{Re_c}$ is analogous to that of $V_{\Delta\text{OSPL}}^{\alpha_{\text{geom.}}}$ (see equation (3)). For conciseness, only one case (at $\alpha_{\text{geom.}} = 6^\circ$) is given in Figure 11 as an example. It can clearly be seen that the metal-foam TE with $d_c = 0.8$ mm shows the largest $V_{\Delta\text{OSPL}}^{Re_c}$ while

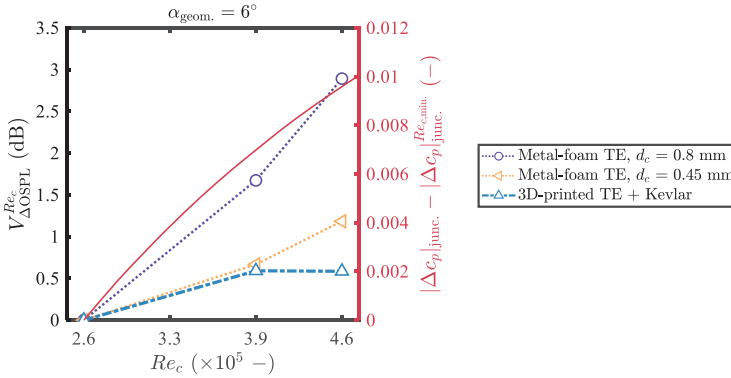


Figure 11. Noise reduction variability with respect to the chord-based Reynolds number of various permeable TE inserts at a geometrical angle of attack of 6 degree relative to the noise reduction at the lowest chord based Reynolds number.

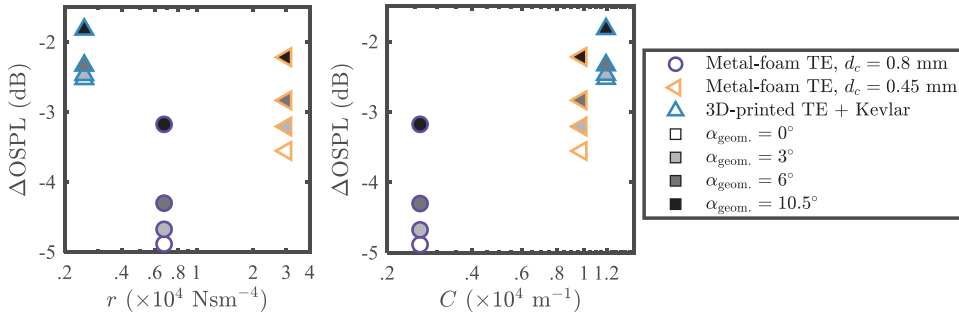


Figure 12. Noise attenuation of the airfoil with various permeable TE inserts at the chord-based Reynolds number of $Re_c = 4.6 \times 10^5$ and various geometrical angles of attack as functions of the flow resistivity (left) and the form drag coefficient (right).

the Kevlar-covered 3D-printed TE insert gives the lowest $V_{\Delta OSPL}^{Re_c}$. Again, as $|\Delta c_p|_{junc.}$ increases with Re_c , the magnitude of $V_{\Delta OSPL}^{Re_c}$ seems to vary inversely with the form drag coefficient C of the permeable material as for $V_{\Delta OSPL}^{2_{geom.}}$ discussed previously. To further address this observation, the next section examines the links between the characterized permeable material properties and the broadband noise attenuation, including its variability with $\alpha_{geom.}$ and Re_c .

Material properties and noise attenuation characteristics

In Figure 12, the parameter $\Delta OSPL$ indicating the overall noise attenuation with respect to the reference solid TE is plotted as functions of r (left) and C (right) for the permeable TE inserts examined. In this case, data is taken from $Re_c = 4.6 \times 10^5$. When only the metal-foam TE inserts are considered, it can be seen that the parameter $\Delta OSPL$ varies proportionally with r and C , meaning that when the flow resistivity r or the form drag coefficient C increases, less noise attenuation is obtained. However, once the Kevlar-covered 3D-printed TE insert is considered together with the metal-foam TE inserts, the same observation no

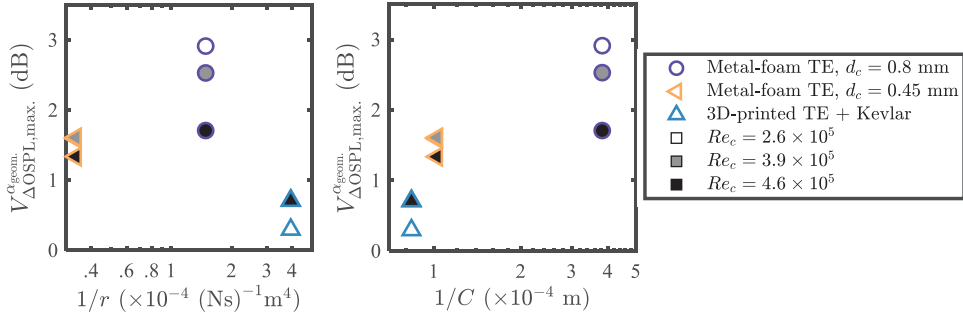


Figure 13. Maximum noise attenuation variability with the geometrical angle of attack of the airfoil with various permeable TE inserts at various chord-based Reynolds numbers as functions of the flow resistivity (left) and the form drag coefficient (right).

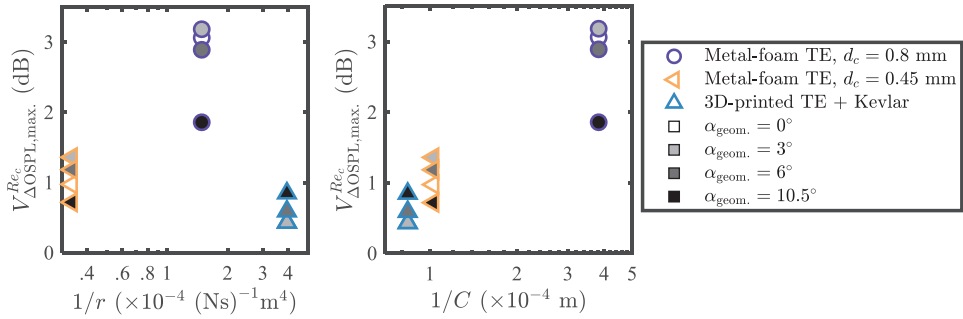


Figure 14. Maximum noise attenuation variability with the chord-based Reynolds number of the airfoil with various permeable TE inserts at various geometrical angles of attack as functions of the flow resistivity (left) and the form drag coefficient (right).

longer holds for the flow resistivity r as shown in Figure 12 (left). Interestingly, the lower noise attenuation capability can still be related to the increase of the form drag coefficient C when the different permeable material topologies are considered altogether.

Following the same format as Figure 12, Figures 13 and 14 relate the material properties to the maximum noise attenuation variability with $\alpha_{\text{geom.}}$ and Re_c , $V_{\Delta\text{OSPL,max}}^{\alpha_{\text{geom.}}}$ and $V_{\Delta\text{OSPL,max}}^{Re_c}$, respectively. A clear increase of $V_{\Delta\text{OSPL,max}}^{\alpha_{\text{geom.}}}$ and $V_{\Delta\text{OSPL,max}}^{Re_c}$ with the inverse of C can be seen in the right subfigures, confirming the observation made in the previous section. Increasing the form drag coefficient C increases the material's ability to withstand the cross flow due to the pressure gradient between the suction and the pressure sides, which strenghtens as $\alpha_{\text{geom.}}$ and/or Re_c increase as illustrated in Figures 10 and 11. Prevention of this possible cross flow could help to sustain the effectiveness of the noise attenuation mechanisms and therefore keep the variability low. Again, when comparing all the permeable TE insert cases, no clear relations of $V_{\Delta\text{OSPL,max}}^{\alpha_{\text{geom.}}}$ and $V_{\Delta\text{OSPL,max}}^{Re_c}$ can be drawn to the inverse of r as shown in the left subfigures.

This section has demonstrated that, while the flow resistivity may be related to the ΔOSPL and its variabilities for materials belonging to the same topological group, e.g. porous metal-foams, at a given Re_c and $\alpha_{\text{geom.}}$, it cannot directly be linked to the ΔOSPL nor its variability with $\alpha_{\text{geom.}}$ and Re_c when multiple permeable material types are considered

altogether. Instead, the form drag coefficient C shows a clearer link to the overall noise attenuation ΔOSPL , including its variability with $\alpha_{\text{geom.}}$ and Re_c , which can be generalized even though the permeable material topologies are different.

Therefore, a design implication with regards to the permeable material characteristics could be drawn from this finding. The permeable material topology for the permeable TE should be realized such that a high form drag coefficient C is achieved in order to ensure its low variability of noise attenuation performance. Then, without major alterations to the topology, the overall permeability (inverse of r) shall carefully be increased to maximize the broadband noise attenuation. As an example, for the present Kevlar-covered 3D-printed topology, the latter could be achieved by enlarging the size of the 3D-printed hexagonal voids.

From the material characterization perspective, considering the pressure drop curve in Figure 6 (left), the ‘ideal’ permeable material based on the design implication is represented by any material that provides a slow increase of $\Delta p/t$ for low values of v_d (dominated by the low r), similar to the ‘No Kevlar’ curve. When v_d increases, $\Delta p/t$ shall increase more rapidly due to the influence of the high C , similar to the ‘With Kevlar’ curve.

Source map analysis

The source maps for the 1/3-octave frequency band centered at 1 kHz, $Re_c = 2.6 \times 10^5$ ($St_{\delta_s^*|_{\text{TE.ref.}}} \approx 0.12$), are presented in Figure 15 at $\alpha_{\text{geom.}} = 0^\circ$. The SPLs shown are ΔSPLs relative to the ‘reference maximum’ SPL for the solid TE case, i.e. $\Delta\text{SPL} = \text{SPL} - \text{SPL}_{\text{ref.,max.}}$. The airfoil boundary is shown analogously to Figure 4. In addition, a source map of the empty test section at the same flow condition and 1/3-octave frequency band is shown as a baseline.

The most dominant noise source can clearly be seen around the TE region in all the source maps where the airfoil is present. The relative levels among the maps visualize the TBL-TE noise attenuation as discussed previously. Additionally, the chordwise locations where the maximum SPL is found $\bar{X}_{\text{SPL}_{1/3}^{\text{max.}}}/c$ are marked by the solid lines for the spanwise extent as wide as the ROI.

Prior to further discussions, it is important to note that the Rayleigh resolution limit at this particular condition is approximately $1.1c$, meaning that sound sources with a physical spacing of less than $1.1c$ cannot be discerned. This distance is much larger than the TE insert extent of $0.2c$. Therefore, one must not deduce that the noise source seen is the only actual source. However, all the presented cases are subjected to the same uncertainty, and the apparent source localization shown in the maps still gives a good implication of the chordwise location where the noise scattering is dominant. Thus, relative comparisons of these locations among the different cases are still valid.

For the solid TE, the dominant noise source appears to align with the trailing edge. However, the dominant noise source appears to shift upstream to a location close to the junction between the solid and the permeable extents of the airfoil for the metal-foam TE cases. The distance with which the dominant noise source shifts upstream for the metal-foam TE cases seems to increase with the increasing d_c , i.e. permeability. The observation confirms what has been reported in a previous study,²¹ suggesting that scattering of noise on metal-foam TE inserts is distributed along the TE insert, resulting in a relatively weaker scattering at the edge. On the other hand, for the Kevlar-covered 3D-printed TE case, the dominant noise source still appears to be at the trailing edge in a more similar way to the solid TE case. This

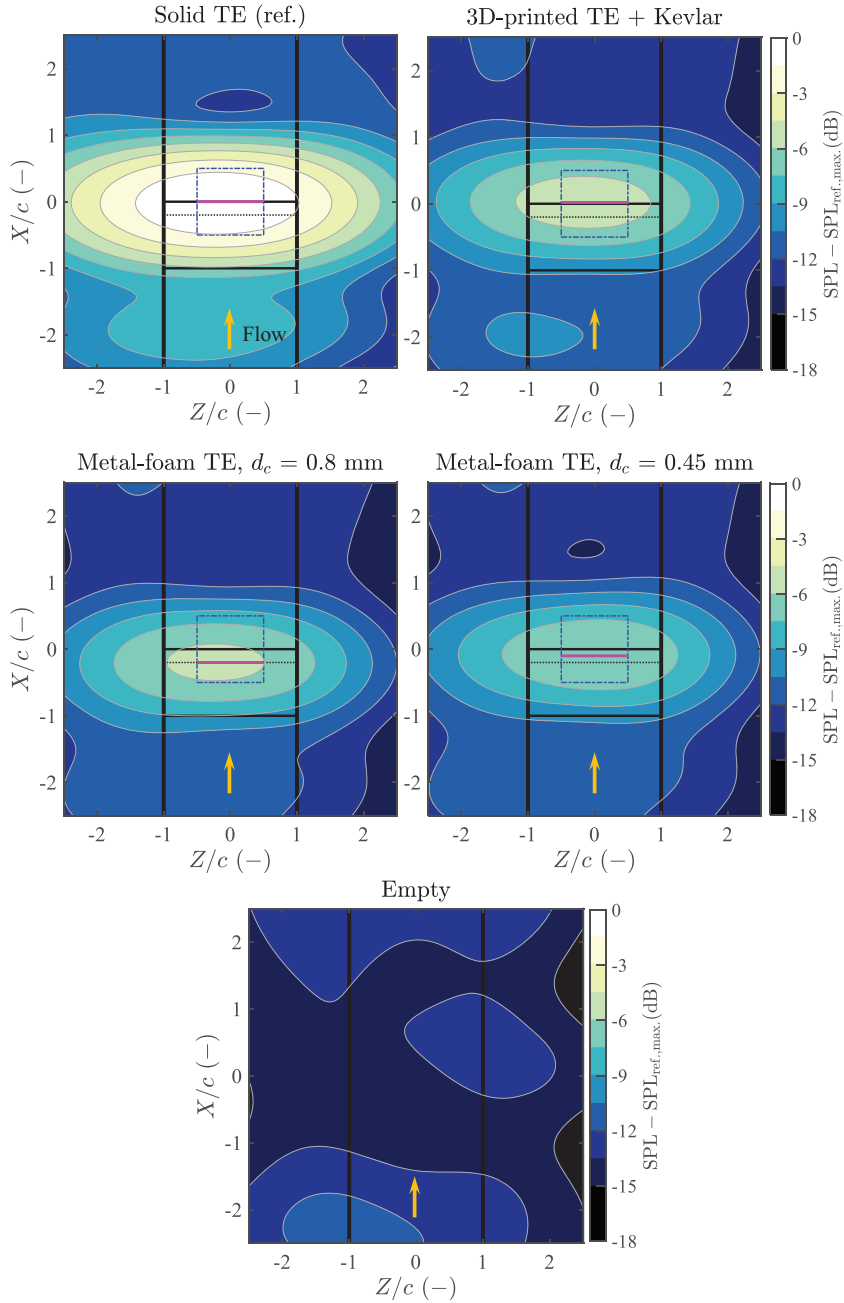


Figure 15. Source maps showing the relative SPL at $Re_c = 2.6 \times 10^5$ ($St_{\delta_1|_{TE,ref.}} \approx 0.12$) and $\alpha_{geom.} = 0^\circ$ for various permeable TE inserts. The levels are relative to the maximum SPL of the ‘reference’ solid TE case ($SPL_{ref.,max.}$), i.e. $\Delta SPL = SPL - SPL_{ref.,max.}$.

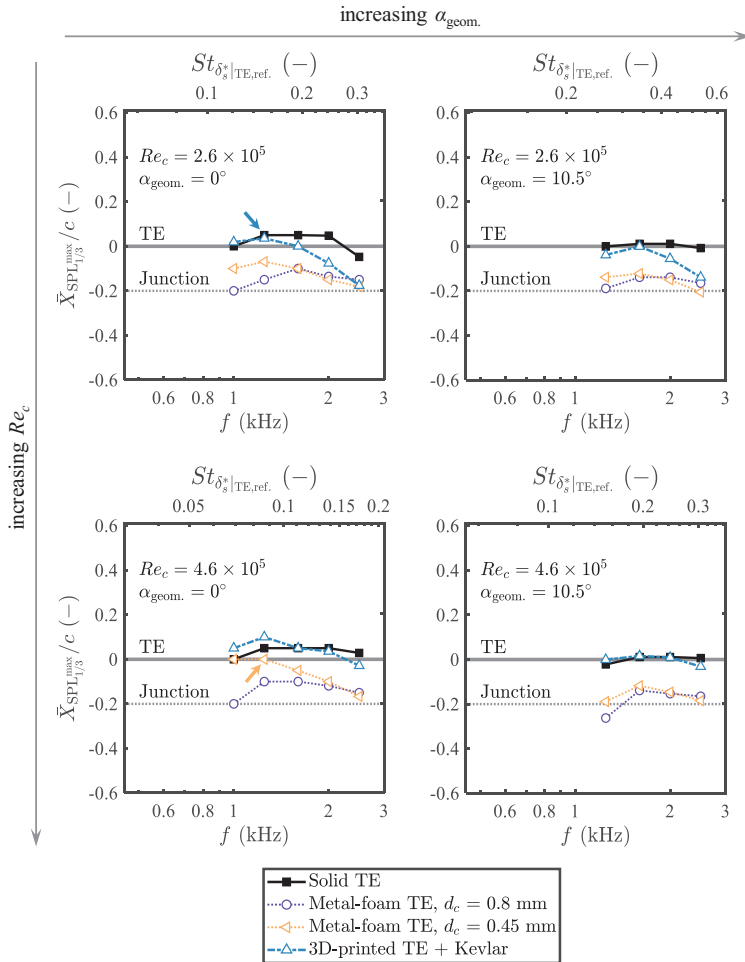


Figure 16. Streamwise locations of the maximum SPL from the source maps per frequency at different combinations of chord-based Reynolds numbers and geometrical angles of attack relative to the locations of the trailing edge (TE) and the junction between the solid and the permeable extents of the airfoil.

suggests that, although noise scattering along the permeable Kevlar-covered 3D-printed TE insert may exist, the noise still scatters most dominantly from the trailing edge.

To broaden the observation, the plots in Figure 16 show the averaged chordwise distance where the maximum SPL is found, $\bar{X}_{\text{SPL}_{1/3}^{\text{max}}}/c$, with respect to the frequency for $Re_c = 2.6 \times 10^5$ and 4.6×10^5 , and $\alpha_{\text{geom.}} = 0^\circ$ and 10.5° . The locations of the trailing edge and the junctions are marked for reference. To avoid interference of the noise source from the nozzle due to the resolution limit, only the results at sound frequencies above 1 kHz are presented.

For the solid TE case, $\bar{X}_{\text{SPL}_{1/3}^{\text{max}}}/c$ aligns approximately with the trailing edge. However, for the metal-foam TE cases, $\bar{X}_{\text{SPL}_{1/3}^{\text{max}}}/c$ is still localized relatively more upstream as observed previously. For most frequencies, $\bar{X}_{\text{SPL}_{1/3}^{\text{max}}}/c$ of the Kevlar-covered 3D-printed TE follows that of the solid TE case closely.

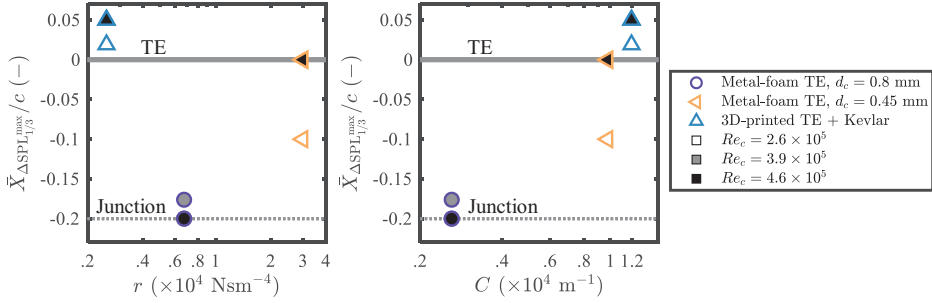


Figure 17. Streamwise locations of the maximum ΔSPL given by various permeable TE inserts at various chord-based Reynolds numbers at zero-degree geometrical angle of attack as functions of the flow resistivity (left) and the form drag coefficient (right).

The trend still holds for $\alpha_{\text{geom.}} = 10.5^\circ$. Noticably, for the metal-foam TE insert case with $d_c = 0.45 \text{ mm}$, $\bar{X}_{\text{SPL}_{1/3}^{\text{max}}}/c$ appears to shift even slightly further upstream. This is likely because of the relatively more dominant noise scattering close to the junction induced by the larger pressure gradient between the suction and the pressure sides at nonzero $\alpha_{\text{geom.}}$.

Therefore, localization of the dominant sound source could again be linked to the ability of the permeable material to withstand the pressure gradient, characterized by the form drag coefficient C . To confirm this, Figure 17 shows the averaged streamwise location at the frequency where the maximum noise attenuation (ΔSPL) is obtained $\bar{X}_{\Delta\text{SPL}_{1/3}^{\text{max}}}/c$ with respect to the flow resistivity r and the form drag coefficient C . In analogy to the observations in the previous section, a clear dependence of the distance of the dominant noise source from the junction and C is identified, meaning that the higher the form drag coefficient of the permeable material, the further the dominant noise scattering source is from the impermeable-permeable junction.

By examining the locations of the dominant noise scattering source with respect to the frequency, an observation can also be made regarding the roughness noise. Figure 16 is arranged in accordance with Figure 9. For the permeable TE cases at high frequencies, it is notable that the frequency at which the $\Delta\text{SPL}_{1/3}$ starts to inflect to the noise increase direction in Figure 9 is approximately the same as the frequency at which $\bar{X}_{\text{SPL}_{1/3}^{\text{max}}}/c$ starts to inflect from the TE to a more upstream location in Figure 16. For example, for the metal-foam TE insert case with $d_c = 0.45 \text{ mm}$ at $Re_c = 4.6 \times 10^5$ and $\alpha_{\text{geom.}} = 0^\circ$, the $\Delta\text{SPL}_{1/3}$ curve in Figure 9 starts to inflect at $f \approx 1.25 \text{ kHz}$, approximately the same frequency as the frequency at which $\bar{X}_{\text{SPL}_{1/3}^{\text{max}}}/c$ in Figure 16 starts to inflect from the TE to the upstream direction. Similarly, the Kevlar-covered 3D-printed TE insert also exhibits this behavior at the same frequency when $Re_c = 2.6 \times 10^5$ and $\alpha_{\text{geom.}} = 0^\circ$. The frequencies where these mutual inflections are found are annotated by the arrows in both Figures 9 and 16. This correlation interestingly visualizes the gradual dominance of the surface roughness noise over the noise scattered at the trailing edge as the frequency increases.

Drag coefficients

The wake profiles measured by the wake rake at a distance of $2c$ downstream of the airfoil trailing edge along a $0.5c$ spanwise traversing distance are shown in Figure 18. The profiles are shown in terms of the measured dynamic pressure deficit, where the dynamic pressure is

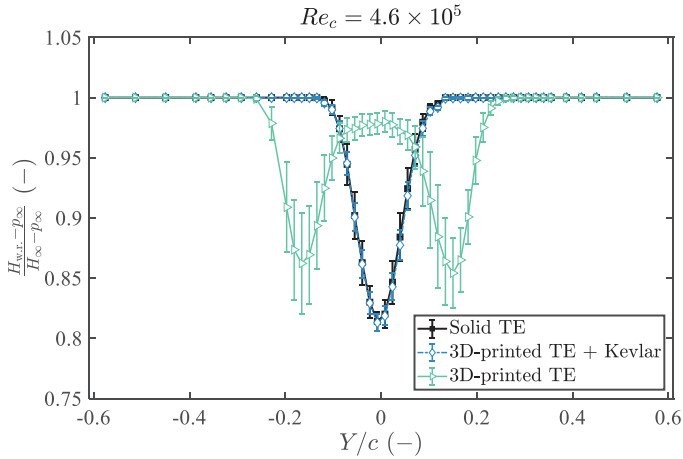


Figure 18. Wake profiles captured downstream of the airfoil with different TE inserts at $Re_c = 4.6 \times 10^5$ and $\alpha_{\text{geom.}} = 0^\circ$.

defined as the difference between the total pressure H and the static pressure p . The subscripts w.r. and ∞ denote the measurement locations at the wake rake and the free stream, respectively. The profiles are measured at $Re_c = 4.6 \times 10^5$ and $\alpha_{\text{geom.}} = 0^\circ$. Only the cases for the solid TE, Kevlar-covered 3D-printed TE, and 3D-printed TE are given to clearly demonstrate the effect of Kevlar application.

Notably, the wake profile downstream of the airfoil with the 3D-printed TE insert without the Kevlar sheet shows two regions with dynamic pressure deficit: downstream of the suction and pressure sides of the airfoil. The regions with the dynamic pressure deficit are likely to result from vortices travelling downstream. In addition, the relatively high deviations suggest that the two regions with the dynamic pressure deficit may probably not exist at the same instance of time. Instead, the dynamic pressure deficit region location alternates between positive and negative Y/c , i.e. downstream of the suction and the pressure sides. Combining this speculation with the previously discussed tonal noise generation unique to this TE insert case, the wake profile strongly suggests existence of the vortex shedding^{1,18,31} starting from the junction between the solid and the permeable parts of the airfoil. In turn, c_D cannot be derived from the momentum deficit in the wake for this particular case due to this unsteadiness. For the remaining cases, the drag coefficient for any given spanwise measurement location is calculated by integrating the momentum deficit (written in terms of the measured pressures) across the wake as^{48,52,53}

$$c_D = 2 \int_{\text{wake}} \sqrt{\frac{H_{\text{w.r.}} - p_{\text{w.r.}}}{H_\infty - p_\infty}} \left(1 - \sqrt{\frac{H_{\text{w.r.}} - p_\infty}{H_\infty - p_\infty}} \right) d\frac{Y}{c} \quad (4)$$

The box plots in Figure 19 show the measured drag coefficients for all the TE insert cases considered and all Re_c collected along the spanwise traversing range of the wake rake. The geometrical angles of attack are $\alpha_{\text{geom.}} = 0^\circ$ and $\alpha_{\text{geom.}} = 10.5^\circ$ for the upper and lower subfigures, respectively. For a reasonable comparison, the distribution of the measured

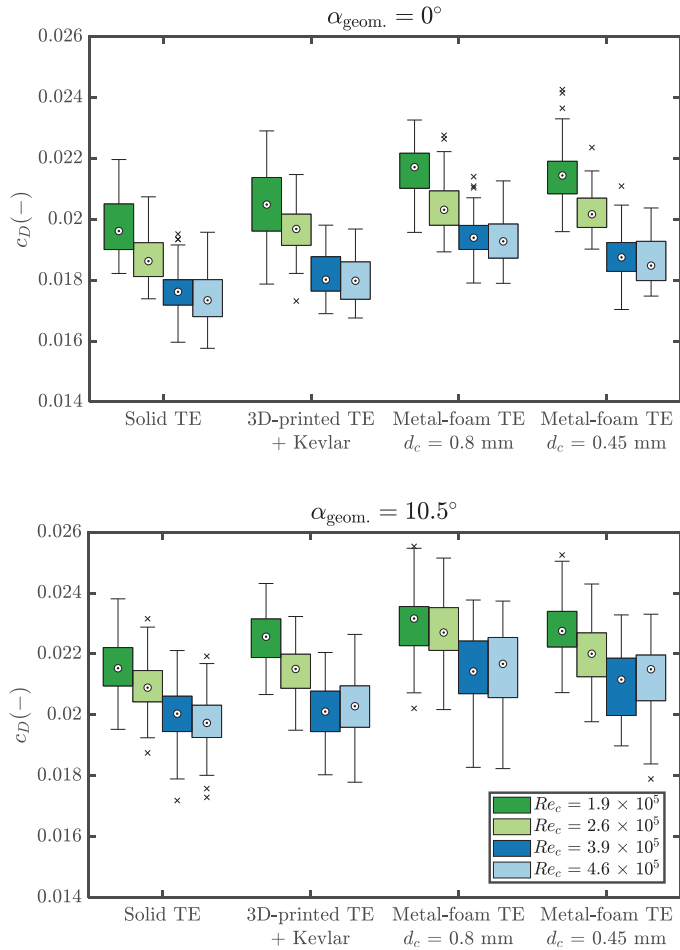


Figure 19. Drag coefficients of the NACA 0018 airfoil with various TE inserts for four different chord-based Reynolds number and geometrical angles of attack of 0° (upper) and 10.5° (lower).

c_D from all the spanwise location is given in the box plot format rather than a single average value since the measured c_D may vary in the spanwise direction for the permeable TE, especially the porous metal foam which have a random topology. The metal-foam TE with $d_c = 0.8$ mm shows the values of c_D followed by the metal-foam TE with $d_c = 0.45$ mm. This can be attributed to the friction drag caused by the rough surface of the metal foams; a larger d_c leads to a rougher surface and thus a higher c_D . Analysis of Variance⁵⁴ and, subsequently, pairwise t-tests⁵⁵ within a confidence interval of 95% (with the Bonferroni correction⁵⁶ applied) have been carried out to objectively assess the difference of the c_D distribution presented in Figure 19. It is found that the c_D of the airfoil with both metal-foam TE insert cases are significantly higher than that of the solid airfoil (P -value $< .01$). Among all the permeable TE insert cases tested, the Kevlar-covered 3D-printed TE seems to give the slightest increase of c_D compared to the solid TE due to the relatively smooth Kevlar surface covering the rather large 3D-printed pores under the Kevlar sheet. In

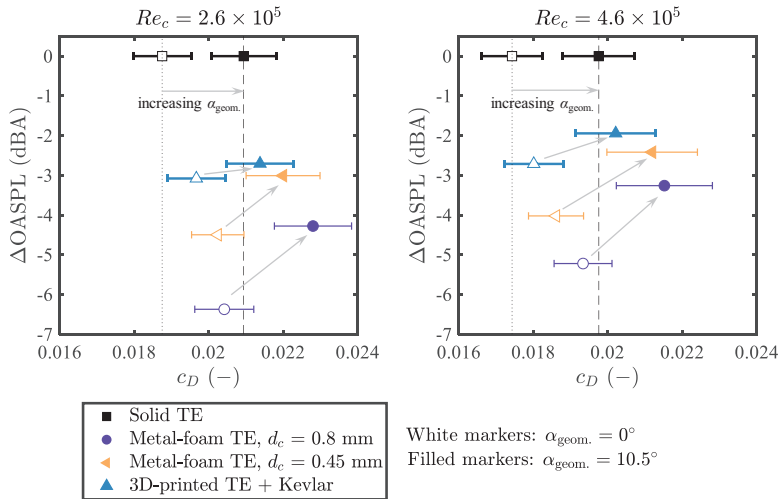


Figure 20. Comparison of noise attenuation and drag coefficients provided by all the permeable TE inserts at different combinations of the chord based Reynolds numbers and geometrical angles of attack.

some cases, such as for $Re_c \leq 2.6 \times 10^5$ and $\alpha_{\text{geom.}} = 10.5^\circ$, this increment of c_D is insignificant (P -value $> .05$) compared to the solid TE. The c_D of the Kevlar-covered 3D-printed TE case is significantly lower than those of the metal-foam TE cases (P -value $< .01$). This confirms that the relatively smooth Kevlar surface provides an evident mitigation of surface drag compared to the metal foams. The mitigation of the surface drag could be achieved by the Kevlar sheet to an extent that the difference of the friction drag between the baseline solid TE and the Kevlar-covered permeable TE insert is negligible.

Summary and derivation of permeable TE insert design concept

The noise attenuation and drag results are combined in Figure 20 where scatter plots of the drag coefficient c_D and the difference of the Overall A-weighted Sound Pressure Levels (OASPL), ΔOASPL , of every TE insert case for $Re_c = 2.6 \times 10^5$ and 4.6×10^5 , and $\alpha_{\text{geom.}} = 0^\circ$ and 10.5° are presented. In this plot, ΔOASPL , defined in the same manner as ΔOSPL , is used to give an implication on perception of noise attenuation in real applications. Nevertheless, for the given frequency range, the A-weighting does not alter the SPL for more than 2 dB and the same observations as discussed previously still hold. The plots visualize the trade-off between the noise attenuation and the aerodynamics performance, the drag in this case. For the metal-foam TE cases tested, additional noise reduction comes at a cost of increasing c_D . The metal-foam TE insert case with $d_c = 0.8$ mm attenuates approximately 3.5 to 6.5 dBA of noise while $d_c = 0.45$ mm attenuates approximately 2.5 to 4.5 dBA. The aforementioned large variability of the noise attenuation with the angle of attack found in the metal-foam cases can also be seen clearly in the figure. This variability is observably larger than that of the Kevlar-covered 3D-printed TE case which gives a rather constant noise attenuation of 2 to 3 dBA over the considered range of $\alpha_{\text{geom.}}$. This results in a comparable noise attenuation between the Kevlar-covered 3D-printed TE insert and the metal-foam TE inserts with $d_c = 0.45$ mm at $\alpha_{\text{geom.}} = 10.5^\circ$. It has been found that the

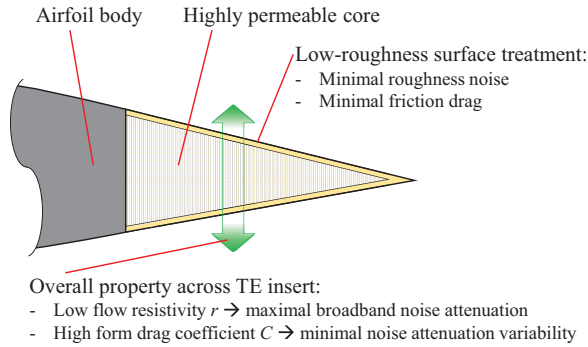


Figure 21. Proposed TE insert design concept for TBL-TE noise attenuation based on findings in the present study.

ranking of the noise attenuation and its variability are inversely proportional to the form drag coefficient C of the permeable materials. The plots also visualize the significant reduction of c_D by the Kevlar-covered 3D-printed TE compared to the metal-foam TE insert cases. At $\alpha_{\text{geom.}} = 10.5^\circ$, it can be seen that the increment of c_D by the Kevlar-covered 3D-printed TE insert is infinitesimal, compared to the solid TE.

By taking into account all the findings discussed so far, a general design guideline for the permeable TE insert topology is derived in Figure 21. This concept features a low-roughness surface treatment which has been proven to help mitigate the surface roughness noise and the friction drag increase. In addition, across the TE insert, a combination of a low flow resistivity r for maximal broadband noise attenuation and high form drag coefficient C for minimal variability of the noise attenuation with $\alpha_{\text{geom.}}$ and Re_c shall be realized. One way to achieve these features is by covering a highly permeable core material with a smooth material having a high form drag coefficient. This paper has shown that the present Kevlar-covered 3D-printed perforated topology is a possible topology which could provide the aforementioned features altogether. Nevertheless, the links between the permeable material characteristics and the aeroacoustic characteristics of an airfoil equipped with it presented in this paper have helped to formulate a generic guideline for the permeable TE insert topological design. Therefore, any permeable material combinations other than the Kevlar-covered 3D-printed perforated channels could also be employed to achieve the same effects, as long as the features prescribed in Figure 21 are fulfilled.

Conclusions and outlook

This paper studies an approach of turbulent boundary layer trailing-edge (TBL-TE) noise mitigation by integrating a simple permeable topology design concept represented by the Kevlar-covered 3D-printed structure into the trailing edge of an airfoil. An experimental study in an open-jet anechoic wind tunnel featuring a NACA 0018 airfoil with a TE insert made of the Kevlar-covered 3D-printed perforated structure was carried out. The results have been compared to those for the same airfoil with a solid TE insert and conventional porous metal-foam TE inserts. The chord-based Reynolds number Re_c was within 1.9×10^5 and 4.6×10^5 and the geometrical angle of attack $\alpha_{\text{geom.}}$ was varied between 0° and 10.5° .

Characterization of the Kevlar-covered 3D-printed permeable topology has shown that the present topology gives an unconventional combination of flow resistivity r and form drag coefficient C . Unlike other conventional permeable materials of which C increases gradually with increasing r , the Kevlar-covered 3D-printed permeable topology gives a drastic increase of C (the highest value among all the permeable materials tested) while the value of r is minimal.

The Kevlar-covered 3D-printed TE provides a broadband TBL-TE noise reduction up to approximately 5 dB as compared to the reference solid airfoil. Although the reduction is not as much as that achieved by the porous metal-foam TE inserts, the reduction is found in a wider range of frequency considered. This is the consequence of the Kevlar sheet exhibiting negligible surface roughness as compared to the metal-foam surface. Apart from the mitigation of the roughness noise, the Kevlar sheet is also found to play an important role in mitigating the tonal noise. This finding suggests that a permeable material with a low r can still be employed as a TE insert for an airfoil without a risk of producing the tonal noise, as long as C is large enough.

Unlike the airfoil with the porous metal-foam TE inserts of which the noise attenuation capability varies strongly with increasing airfoil loading, the airfoil with the Kevlar-covered 3D-printed TE insert clearly gives a lower variability. Within the range of Re_c and α_{geom} considered, this TE insert gives a noise attenuation variability lower than 1 dB, while the metal-foam TE inserts give a maximum variability up to 3 dB.

When relating the characterized permeable material properties to the noise attenuation and its variability, it has been found that, when different permeable topologies are compared, the form drag coefficient C shows a clearer relation to those aeroacoustic behaviors than the resistivity r . The broadband noise attenuation as well as the noise attenuation variabilities are found to vary inversely with C . Additionally, analysis of the source maps has also shown the dominant noise scattering source shifts further away from the solid-permeable junction when C of the permeable material increases.

Lastly, the drag coefficients provided by the airfoil with the Kevlar-covered 3D-printed TE insert is significantly lower than that provided by the metal-foam TE inserts due to the relatively lower surface roughness. In many cases, especially at high Re_c and α_{geom} , the drag increment given by this proposed TE insert compared to a solid airfoil is insignificant.

The aeroacoustic findings, in combination with their links to the material properties, have led to a design guideline for a permeable TE insert topology for TBL-TE noise attenuation. The features that the design needs to fulfill are:

- In the direction linking the suction and the pressure sides, the permeable material shall have a combination of a low flow resistivity but a high form drag coefficient to achieve maximal broadband noise attenuation while having a low variability of noise attenuation with the airfoil loading.
- The surface roughness of the permeable insert shall be negligible, compared to the solid extent of the airfoil, in order to have a minimal increment of the friction drag as well as the roughness noise.

When these requirements are fulfilled, a promising trade-off between the noise attenuation and the aerodynamics penalty, i.e. drag increase, is obtained. Apart from the significantly low surface roughness, noise attenuation by a topology as such also appears to be less sensitive to the increasing airfoil loading, compared to the conventional porous metal

foams. A simple permeable material combination such as the Kevlar-covered 3D-printed permeable structure considered in this paper could be one, but indeed not only, possible realization to fulfill those requirements.

Crucial elements for future studies include realization of strong, yet highly permeable, topologies and materials for the inner part of the proposed TE insert design concept. In addition, performance of the proposed concept on a realistic wind turbine to verify its noise attenuation capability as well as effects of the streamwise permeable TE insert length on both aerodynamic and aeroacoustic performances shall also be investigated.

Acknowledgements

The authors would like to acknowledge Alejandro Rubio Carpio and Reza Hedayati for sharing the permeable TE inserts and material samples.


Declaration of conflicting interests

The author(s) declared no potential conflicts of interest with respect to the research, authorship, and/or publication of this article.

Funding

The author(s) disclosed receipt of the following financial support for the research, authorship, and/or publication of this article: This work is a part of the Innovative PERmeable Materials for Airfoil Noise Reduction (IPER-MAN) project funded by the Netherlands Organisation for Scientific Research (NWO) and the associating users, project number 15452.

ORCID iD

Salil Luesutthiviboon  <https://orcid.org/0000-0002-0563-9431>

References

1. Brooks TF, Pope DS and Marcolini MA. *Airfoil self-noise and prediction*. USA: NASA Reference Publication, 1989.
2. Basner M, Babisch W, Davis A, et al. Auditory and non-auditory effects of noise on health. *The Lancet* 2014; 383: 1325–1332.
3. Hansell AL, Blangiardo M, Fortunato L, et al. Aircraft noise and cardiovascular disease near Heathrow airport in London: small area study. *Bmj* 2013; 347: f5432–f5432.
4. World Health Organization. *Environmental noise guidelines for the European region*. Geneva: WHO, 2018.
5. Oerlemans S and Fuglsang P. Low-noise wind turbine design. In: EWEA Workshop ‘Wind turbine noise: From source to receiver’, Said Business School, Oxford, UK, 11–12 December 2012.
6. Pomerantz D. Size matters: the next big thing in wind turbines, www.ge.com/reports/size-matters-next-big-thing-wind-turbines/ (2017, accessed 1 October 2018).
7. Curle N. The influence of solid boundaries upon aerodynamic sound. *Proc R Soc Lond A* 1955; 231: 505–514.
8. Williams JF and Hall L. Aerodynamic sound generation by turbulent flow in the vicinity of a scattering half plane. *J Fluid Mech* 1970; 40: 657–670.
9. Finez A, Jacob M, Jondeau E, et al. Broadband noise reduction with trailing edge brushes. In: *16th AIAA/CEAS aeroacoustics conference*, Stockholm, Sweden, 7–9 June 2010, AIAA 2010–3980.
10. Arce León CA, Merino Martínez R, Ragni D, et al. Boundary layer characterization and acoustic measurements of flow-aligned trailing edge serrations. *Exp Fluids* 2016; 57: 182.

11. Oerlemans S, Fisher M, Maeder T, et al. Reduction of wind turbine noise using optimized airfoils and trailing-edge serrations. *AIAA J* 2009; 47: 1470–1481.
12. Gruber M, Azarpeyvand M. and Joseph PF. Airfoil trailing edge noise reduction by the introduction of sawtooth and slitted trailing edge geometries. In: *20th international congress on acoustics*, Sydney, Australia, 23–27 August 2010.
13. Geyer TF, Sarradj E and Fritzsche C. Measurement of the noise generation at the trailing edge of porous airfoils. *Exp Fluids* 2010; 48: 291–308.
14. Geyer TF, Sarradj E and Fritzsche C. Porous airfoils: noise reduction and boundary layer effects. In: *15th AIAA/CEAS aeroacoustics conference*, Miami, FL, USA, 11–13 May 2009, AIAA 2009–3392.
15. Sarradj E and Geyer TF. Noise generation by porous airfoils. In: *13th AIAA/CEAS aeroacoustics conference*, Rome, Italy, 21–23 May 2007, AIAA 2007–3719.
16. Rubio Carpio A, Merino Martínez R, Avallone F, et al. Broadband trailing-edge noise reduction using permeable metal foams. In: *INTER-NOISE Conference*, Hong Kong, 27–30 August 2017. Washington DC: Institute of Noise Control Engineering.
17. Herr M. Design criteria for low-noise trailing-edges. In: *13th AIAA/CEAS aeroacoustics conference*, Rome, Italy, 21–23 May 2007, AIAA 2007–3470.
18. Herr M, Rossignol KS, Delfs J, et al. Specification of porous materials for low-noise trailing-edge applications. In: *20th AIAA/CEAS aeroacoustics conference*, Atlanta, Georgia, 16–20 June 2014, AIAA 2014–3041.
19. Geyer TF and Sarradj E. Trailing edge noise of partially porous airfoils. In: *20th AIAA/CEAS aeroacoustics conference*, Atlanta, Georgia, 16–20 June 2014, AIAA 2014–3039.
20. Rubio Carpio A, Merino Martínez R, Avallone F, et al. Experimental characterization of the turbulent boundary layer over a porous trailing edge for noise abatement. *J Sound Vibr* 2019; 443: 537–558.
21. Rubio Carpio A, Avallone F, Ragni D, et al. Mechanisms of broadband noise generation on metal foam edges. *Physics Fluids* 2019; 31: 105110.
22. Hajian R and Jaworski JW. The steady aerodynamics of aerofoils with porosity gradients. *Proc Math Phys Eng Sci* 2017; 473: 20170266.
23. Bae Y and Moon YJ. Effect of passive porous surface on the trailing-edge noise. *Phys Fluids* 2011; 23: 126101.
24. Darcy HPG. *Les Fontaines publiques de la ville de Dijon. Exposition et application des principes à suivre et des formules à employer dans les questions de distribution d'eau, etc.* V. Dalamont, 1856. <https://gallica.bnf.fr/ark:/12148/bpt6k624312/f1n657.pdf>
25. Forchheimer P. Wasserbewegung durch Boden. *Zeitz. ver. Deutsch Ing.* vol. 45, 1901, pp. 1782–1788.
26. Dukhan N and Patel KP. Entrance and exit effects for fluid flow in metal foam. *AIP Conf Proc* 2010; 1254: 299–304.
27. Ingham DB and Pop I. *Transport phenomena in porous media*. Amsterdam: Elsevier, 1998.
28. Rubio Carpio A, Avallone F, Ragni D, et al. 3D-printed perforated trailing edges for broadband noise abatement. In: *25th AIAA/CEAS aeroacoustics conference*, Delft, the Netherlands, 20–23 May 2019, AIAA 2019–2458.
29. Ali SAS, Azarpeyvand M and da Silva CRI. Trailing-edge flow and noise control using porous treatments. *J Fluid Mech* 2018; 850: 83–119.
30. Herr M and Reichenberger J. In search of airworthy trailing-edge noise reduction means. In: *17th AIAA/CEAS aeroacoustics conference*, Portland, OR, USA, 5–8 June 2011, AIAA 2011–2780. Reston: American Institute of Aeronautics and Astronautics.
31. Rubio Carpio A, Avallone F, Ragni D, et al. Quantitative criteria to design optimal permeable trailing edges for noise abatement. *J Sound Vibr* 2020; 485: 115596.

32. Smith B, Camargo H, Burdisso R, et al. Design. And testing of a novel acoustic wind tunnel concept. In: *11th AIAA/CEAS aeroacoustics conference*, Monterey, CA, USA, 23–25 May 2005, AIAA 2005–3053.
33. Devenport WJ, Burdisso RA, Borgoltz A, et al. The kevlar-walled anechoic wind tunnel. *J Sound Vibr* 2013; 332: 3971–3991.
34. Devenport WJ, Burdisso RA, Borgoltz A, et al. Aerodynamic and acoustic corrections for a kevlar-walled anechoic wind tunnel. In: *16th AIAA/CEAS aeroacoustics conference*, Stockholm, Sweden, 7–9 June 2010, AIAA 2010–3749.
35. Ito T, Ura H, Nakakita K, et al. Aerodynamic/aeroacoustic testing in anechoic closed test sections of low-speed wind tunnels. In: *16th AIAA/CEAS aeroacoustics conference*, Stockholm, Sweden, 7–9 June 2010, AIAA 2010–3750.
36. Remillieux M, Crede E, Camargo H, et al. Calibration and demonstration of the new Virginia tech anechoic wind tunnel. In: *14th AIAA/CEAS aeroacoustics conference*, Vancouver, Canada, 5–7 May 2008, AIAA 2008–2911.
37. Merino Martínez R, Rubio Carpio A, Pereira LTM, et al. Aeroacoustic design and characterization of the 3D-printed, open-jet, anechoic wind tunnel of Delft University of Technology. *App Acoustics* 2020; 170: 107504.
38. ECC, Technisches D. *Style 120*, 2009. http://www.ezentrumbilder.de/rg/pdf/td_en_ECC_Style120_E.pdf
39. White FM and Corfield I. *Viscous fluid flow*. volume 3. New York: McGraw-Hill, 2006.
40. Luesutthiviboon S, Malgoezar AMN, Snellen M, et al. Improving source discrimination performance by using an optimized acoustic array and adaptive high-resolution CLEAN–SC beamforming. In: *7th Berlin beamforming conference*, Berlin, Germany, 5–6 March 2018, BeBeC–2018–D07. Berlin: GFaI, e.V.
41. Luesutthiviboon S, Malgoezar AMN, Merino Martínez R, et al. Enhanced HR–CLEAN–SC for resolving multiple closely spaced sound sources. *Int J Aeroacoust* 2019; 18: 392–413.
42. Rayleigh L. XXXI. Investigations in optics, with special reference to the spectroscope. *London, Edinburgh, Dublin Philos Magaz J Sci* 1879; 8: 261–274.
43. Van Veen BD and Buckley KM. Beamforming: a versatile approach to spatial filtering. *IEEE ASSP Mag* 1988; 5: 4–24.
44. Merino Martínez R, Sijtsma P and Snellen M. Inverse integration method for distributed sound sources. In: *7th Berlin beamforming conference*, Berlin, Germany, 5–6 March 2018, BeBeC–2018–S07. Berlin: GFaI, e.V.
45. Sarradj E, Herold G, Sijtsma P, et al. A microphone array method benchmarking exercise using synthesized input data. In: *23rd AIAA/CEAS aeroacoustics conference*, Denver, CO, USA, 5–7 June 2016, AIAA 2017–3719.
46. Merino Martínez R, Sijtsma P, Rubio Carpio A, et al. Integration methods for distributed sound sources. *Int J Aeroacoust* 2019; 18(4–5): 444–469.
47. Timmer W. Two-dimensional low-Reynolds number wind tunnel results for airfoil NACA 0018. *Wind Eng* 2008; 32: 525–537.
48. Barlow JB, Rae WH. and Pope A. *Low-speed wind tunnel testing*. Hoboken, NJ: John Wiley & sons, 1999.
49. Brooks TF, Pope DS. and Marcolini MA Airfoil trailing edge flow measurements and comparison with theory, incorporating open wind tunnel corrections. In: *9th AIAA/CEAS aeroacoustics conference*, Williamsburg, VA, USA, 10–15 October 1984, AIAA 1984–2266. Reston: American Institute of Aeronautics and Astronautics.
50. Drela M. XFOIL: An Analysis and Design System for Low Reynolds Number Airfoils. In: Mueller TJ (ed) *Low Reynolds number aerodynamics*. Berlin: Springer, 1989, pp.1–12.
51. Avallone F, van der Velden WC, Merino Martínez R, et al. Near-wall pressure fluctuations over noise reduction add-ons. In: *23rd AIAA/CEAS aeroacoustics conference*, Denver, CO, USA, June 5–7 2016, AIAA 2017–4171.

52. Houghton EL and Carpenter PW. *Aerodynamics for engineering students*. Amsterdam: Elsevier, 2003.
53. Russo GP. *Aerodynamic measurements: from physical principles to turnkey instrumentation*. Amsterdam: Elsevier, 2011.
54. Scheffe H. *The analysis of variance, volume 72*. Hoboken, NJ: John Wiley & Sons, 1999.
55. Student The probable error of a mean. *Biometrika* 1908; 6: 1–25.
56. Rupert JG, et al. *Simultaneous statistical inference*. Berlin: Springer Science & Business Media, 2012.

Appendix

Notation

A	cross-sectional area (m^2)
C	form drag coefficient (1/m)
c	chord length (m)
c_D	drag coefficient (–)
c_p	pressure coefficient (–)
d_c	cell diameter (m)
f	frequency (Hz)
H	total pressure (Pa)
K	permeability (m^2)
k_B	correction factor (–)
l	airfoil local thickness (m)
p	static pressure (Pa)
Q	volumetric flow rate (m^3/s)
Re_c	chord-based Reynolds number (–)
r	air flow resistivity (Ns/m^4)
St	Strouhal number (–)
t	thickness (m)
U_∞	free-stream velocity (m/s)
V_a^b	variability of a with b (unit of a)
v_d	Darcy velocity (m/s)
X	chordwise/streamwise distance (m)
Y	trailing-edge-normal distance (m)
Z	spanwise distance (m)
α	angle of attack (deg.)
δ^*	displacement thickness (m)
ϵ	angle offset (deg.)
μ	dynamic viscosity ($\text{kg}/(\text{ms})$)
ρ	density (kg/m^3)

Subscripts and superscripts

∞	free-stream condition
'	fundamental frequency
$1/3$	one-third octave
s	suction side

eff. effective
geom. geometrical
junc. junction
max. maximum
min. minimum
ref. reference
w.r. wake rake